6

Numerical Modeling of Analytical Glow Discharges

ANNEMIE BOGAERTS and RENAAT GIJBELS
University of Antwerp, Department of Chemistry, Wilrijk, Belgium

6.1 INTRODUCTION

In order to improve the analytical capabilities of glow discharges, and to study the relation between plasma properties and analytical results, a good insight into the plasma processes is desirable. This can be obtained by, among others, numerical simulations of the behavior of the various plasma species.

There are a large number of papers in the (plasma physics) literature about glow discharge modeling (e.g. [1–14]), but these models were generally developed for other application fields. Indeed, glow discharges and related plasmas are not only used in analytical spectrometry, but also find application in a large number of other fields, e.g. in the semiconductor industry (for etching of surfaces or for the deposition of thin films), in materials technology (for the deposition of protective coatings), as gas lasers, light sources, flat plasma display panels, etc. The models referred to apply generally to other discharge conditions and setups. They focus on different aspects in the plasma (e.g. mainly the electrical characteristics, or plasma instabilities, etc.), and they do not consider the analytically important characteristics (such as sputtered atoms and ions, optical emission intensities, erosion rates, etc.). Nevertheless, these models have appeared to be very useful as a basis to start the numerical modeling of analytical glow discharges. The list of models for analytical glow discharges is rather limited. In addition to the work carried out in our group (e.g. [15,16] and references cited therein), a number of

---

Glow Discharge Plasmas in Analytical Spectroscopy, edited by R.K. Marcus and J.A.C. Broekaert

other groups have performed modeling work for analytical glow discharges, but only to a limited extent [17–21]. Therefore, the data presented in this chapter will mainly stem from our work.

Table 6.1 gives an overview of the different modeling approaches in the literature to describe glow discharge plasmas, with their specific features and drawbacks. A so-called *analytical model* [1,2] is based on deriving suitable equations to describe the plasma behavior. This approach is very fast and can easily predict trends in the behavior of glow discharges. However, it is only a rough approximation, valid for a limited range of conditions. A *fluid model* [3,4] makes use of the first velocity moments of the Boltzmann equation (i.e. continuity equations of particle density, momentum density and energy density) usually coupled to Poisson's equation to obtain a self-consistent electric field distribution. This means that the electric field calculated from Poisson's equation based on the electron and ion charge densities is used in turn to calculate the behavior of these charged plasma species. It is in principle also fairly simple and fast, although it can be tricky to solve the set of coupled differential equations, but it is also approximative. Indeed, it assumes that the plasma species are more or less in equilibrium with the electric field, which means that the energy they gain from the electric field is roughly balanced by the energy they lose due to collisions. This is, for example, not true for the fast electrons in the cathode dark space (CDS). In this region adjacent to the cathode, characterized by a strong electric field, they gain more energy from the electric field than they lose by collisions. Solving the *full Boltzmann equation* [5,6] takes into account the nonequilibrium behavior of the plasma species, but this approach can become

Table 6.1 Different models used in the (plasma physics) literature to describe glow discharge plasmas, with their specific features and limitations.

Model	Short description	Advantage	Disadvantage
Analytical	Simple equations	Simple, fast	Approximation
Fluid	Momentum equations of Boltzmann equation	Simple, fast, self-consistent	Approximation (thermal equilibrium)
Boltzmann	Full Boltzmann equation	Nonequilibrium	Complex
Monte Carlo	Newton's laws + random numbers	Accurate	Long calculation time, not self-consistent
Particle-in-cell	As above + Poisson equation	Accurate + self-consistent	Long calculation time
Hybrid	Combination of above models	Accurate + self-consistent, reduced calculation time	—

mathematically very complicated, especially in more than one dimension. In contrast, *Monte Carlo simulations* [7,8] are mathematically very simple. Indeed, a large number of plasma particles are followed, one after the other. Their trajectories are calculated with Newton's laws and their collisions are treated with random numbers. If a large number of particles are followed in this statistical way, their behavior can be simulated. Because this modeling approach describes the plasma species at the lowest microscopic level, it is very accurate. However, in order to obtain sufficient statistics, a large number of particles have to be simulated, which leads to a long calculation time, especially for slow-moving particles. Moreover, the Monte Carlo model on its own requires the electric field distribution as input value, and therefore is not self-consistent. The latter problem is overcome in the *particle-in-cell method* [9,11], which couples Monte Carlo simulations for the behavior of electrons and ions to the Poisson equation for a self-consistent electric field. However, this approach is even more time consuming than the Monte Carlo approach.

As a method for analytical glow discharges we use a so-called *hybrid model* [12–14], which benefits from the advantages of the various models, and does not suffer so much from the disadvantages. Indeed, it is very accurate since it applies the most accurate Monte Carlo models where needed, namely for fast plasma species, such as fast electrons and ions, and it benefits from a reduced computation time by using faster (fluid) models where possible. This is the case for slow plasma species, such as slow electrons and ions, which are practically in equilibrium with the electric field. Moreover, when the fluid model also incorporates Poisson's equation, the hybrid model also yields self-consistent results. In this chapter, we will give an overview and a brief description of the different models that we have developed for the various plasma species, and discuss some typical results, mainly for direct current (dc), but also radio frequency (rf) and microsecond pulsed discharges.

6.2 DESCRIPTION OF THE MODELS

6.2.1 GENERAL OVERVIEW

The various collision processes in the plasma, described in our hybrid model, are summarized in Table 6.2. It is clear that not all these processes take place to the same extent, but the table tries to give a complete overview, and can be used as a reference when the processes are mentioned later in this paper. A schematic picture of the most important plasma processes can be found elsewhere [22].

Table 6.3 gives an overview of the plasma species considered in our simulations, as well as the different models used to describe these species. We assume that the discharge gas is pure argon and that the cathode is made of pure copper. The argon gas atoms are usually assumed to be at rest, uniformly distributed throughout the discharge, and in general no model is used to describe

Table 6.2 Overview of the collision processes in the plasma described in the models.[a]

Electrons: elastic collisions with argon atoms	$e^- + Ar^0 \rightarrow e^- + Ar^0$
Electrons: ionization of argon atoms or copper atoms or ions (in the ground state or in excited levels)	$e^- + X \rightarrow X^+ + 2e^-$ $(X = Ar^0, Ar^*, Cu^0, Cu^*, Cu^+ \text{ or } Cu^{+*})$
Electrons: two-electron ionization of argon atoms	$e^- + Ar^0 \rightarrow Ar^{2+} + 3e^-$
Electrons: ionization of Ar^+ ions	$e^- + Ar^+ \rightarrow Ar^{2+} + 2e^-$
Electrons: excitation of argon atoms or copper atoms or ions (in the ground state or in excited levels)	$e^- + X \rightarrow e^- + X^{**}$ $(X = Ar^0, Ar^*, Cu^0, Cu^*, Cu^+ \text{ or } Cu^{+*})$
Electrons: de-excitation of argon atomic or copper atomic or ionic excited levels	$e^- + X^* \rightarrow e^- + X^{*\prime} \text{ or } X^0$ $(X^* = Ar^*, Cu^*, \text{ or } Cu^{+*})$
Electrons: Coulomb scattering with other electrons	$e^- + e^- \rightarrow e^- + e^-$
Argon ions: elastic collisions with argon atoms	$Ar^+ + Ar^0 \rightarrow Ar^+ + Ar^0$
Argon ions: symmetric charge transfer with argon atoms	$Ar_f{}^+ + Ar_s^0 \rightarrow Ar_f^0 + Ar_s{}^+$
Argon ions: ionization of argon atoms (in the ground state or in excited levels)	$Ar^+ + Ar^0 \text{ (or } Ar^*) \rightarrow Ar^+ + Ar^+ + e^-$
Argon ions: excitation of argon atoms (in the ground state or in excited levels)	$Ar^+ + Ar^0 \text{ (or } Ar^*) \rightarrow Ar^+ + Ar^{**}$
Argon ions: de-excitation of argon excited levels	$Ar^+ + Ar^* \rightarrow Ar^+ + Ar^{*\prime} \text{ or } Ar^0$
Argon ions: Ar^+ to $Ar_2{}^+$ conversion	$Ar^+ + 2Ar^0 \rightarrow Ar_2{}^+ + Ar^0$
Argon atoms: elastic collisions with argon atoms	$Ar^0 + Ar^0 \rightarrow Ar^0 + Ar^0$
Argon atoms: ionization of argon atoms (in the ground state or in excited levels)	$Ar^0 + Ar^0 \text{ (or } Ar^*) \rightarrow Ar^0 + Ar^+ + e^-$
Argon atoms: excitation of argon atoms (in the ground state or in excited levels)	$Ar^0 + Ar^0 \text{ (or } Ar^*) \rightarrow Ar^0 + Ar^{**}$
Argon atoms: de-excitation of argon excited levels	$Ar^0 + Ar^* \rightarrow Ar^0 + Ar^{*\prime} \text{ or } Ar^0$
Electron–Ar^+ ion radiative recombination	$e^- + Ar^+ \rightarrow Ar^0 \text{ (or } Ar^*) + h\nu$
Electron–Ar^+ (or Ar^{2+} or Cu^+ or Cu^{2+}) ion three-body recombination with an electron as third body	$e^- + X^+ + e^- \rightarrow X^0 \text{ (or } X^*) + e^-$ $(X = Ar, Ar^+, Cu \text{ or } Cu^+)$
Electron–Ar^+ ion three-body recombination with an argon atom as third body	$e^- + Ar^+ + Ar^0 \rightarrow Ar^0 \text{ (or } Ar^*) + Ar^0$
Electron–$Ar_2{}^+$ ion dissociative recombination	$e^- + Ar_2{}^+ \rightarrow Ar^0 \text{ (or } Ar^*) + Ar^0 \text{ (or } Ar^*)$

Table 6.2 (*continued*)

Radiative decay of argon atom, copper atom or ion excited levels	$X^* \rightarrow X^0$ (or $X^{*\prime}$) $+ h\nu$ ($X = Ar$, Cu or Cu^+)
Argon metastable atom–metastable atom ionization	$Ar^*_m + Ar^*_m \rightarrow Ar^+ + Ar^0 + e^-$
Argon metastable atom–metastable atom associative ionization	$Ar^*_m + Ar^*_m \rightarrow {Ar_2}^+ + e^-$
Hornbeck–Molnar associative ionization (for Ar^{**} >14.6 eV)	$Ar^{**} + Ar^0 \rightarrow {Ar_2}^+ + e^-$
Two-body collisions of argon metastable atoms with Ar atoms	$Ar^*_m + Ar^0 \rightarrow Ar^0 + Ar^0$
Three-body collisions of argon metastable atoms with Ar atoms	$Ar^*_m + 2Ar^0 \rightarrow Ar^*_2 + Ar^0$
Cu (sputtered) atoms: elastic collisions with argon atoms → until thermalized	$Cu^0_f + Ar^0 \rightarrow Cu^0 + Ar^0$
Cu atoms: Penning ionization by argon metastable atoms	$Ar^*_m + Cu^0 \rightarrow Ar^0 + Cu^+ + e^-$
Cu atoms: asymmetric charge transfer with Ar^+ ions	$Ar^+ + Cu^0 \rightarrow Ar^0 + Cu^+$
Cu atoms: two-electron asymmetric charge transfer with Ar^{2+} ions	$Ar^{2+} + Cu^0 \rightarrow Ar^0 + Cu^{2+}$
Cu ions: elastic collisions with argon atoms	$Cu^+ + Ar^0 \rightarrow Cu^+ + Ar^0$

[a] Ar^*, $Ar^*{}_m$, $Ar^{*\prime}$, and Ar^{**} denote argon atoms in excited levels, in the metastable levels, in lower excited levels and higher excited levels, respectively. The subscripts f and s indicate fast and slow atoms or ions, respectively. The other symbols are straightforward.

Table 6.3 Overview of the different plasma species considered in the simulations, and the various models used to describe these species.

Plasma species	Model
Ar gas atoms	No model (uniformly distributed + at rest) or gas heating model (dc case)
Fast electrons	Monte Carlo model
Slow electrons	Fluid model
Ar^+, Ar^{2+}, ${Ar_2}^+$ ions	Fluid model
Ar^+ ions in CDS	Monte Carlo model
Fast Ar^0_f atoms in CDS	Monte Carlo model
Ar atoms in various excited levels	Collisional-radiative model
Sputtered Cu atoms: thermalization	Monte Carlo model
Cu atoms and ions in ground state + excited levels	Collisional-radiative model
Cu^+ ions in CDS	Monte Carlo model

their behavior. Nevertheless, we recently developed a model to describe argon gas heating in dc glow discharges, and we calculated a nonuniform gas temperature and hence a nonuniform argon gas density throughout the discharge. The other plasma species are described by either a Monte Carlo, a fluid or a collisional-radiative model. The electrons are split up into a fast and a slow group, depending on their energy. The electrons are called 'fast' when they have enough energy to produce inelastic collisions (i.e. ionization and excitation). The fast electrons, which are not in equilibrium with the electric field, are described with a Monte Carlo model, whereas the slow electrons, which can be considered to be in equilibrium with the electric field, are treated with a fluid approach, together with the argon ions (Ar^+, Ar^{2+} and $Ar_2{}^+$). Moreover, this fluid model incorporates also the Poisson equation, for self-consistent electric field results. Since the Ar^+ ions are not in equilibrium with the strong electric field in the CDS, they are also handled with a Monte Carlo model in this region. Moreover, the fast argon atoms, Ar_f^0, which are created in collisions from the Ar^+ ions, are also simulated with a Monte Carlo model in the CDS. The argon atoms in various excited levels are described with a so-called collisional-radiative model. This is actually a kind of fluid model, which consists of a set of balance equations (one for each excited level) with different production and loss terms. The name 'collisional-radiative' model stems from the fact that the production and loss processes are typically due to collisions or radiative decay (see below).

The sputtering of copper atoms at the cathode is calculated with an empirical equation for the sputtering yield as a function of energy of the bombarding particles, multiplied with the flux energy distributions of the bombarding particles. Immediately after sputtering from the cathode the sputtered copper atoms undergo a thermalization as a result of collisions with the argon gas atoms. This is described with a Monte Carlo model. The further behavior of copper atoms, their ionization and excitation and the behavior of the corresponding copper ions and excited copper atoms and ions is described with a collisional-radiative model. Finally, because the copper ions are not in equilibrium with the electric field in the CDS, they are also described with a Monte Carlo model in this region.

All the models mentioned above are coupled to each other because of the interaction processes between the species, i.e. the output of one model is used as input for the next model, and so on. The models are solved iteratively until final convergence is reached, to obtain an overall picture of the glow discharge. The Monte Carlo models are developed in three dimensions. The fluid and collisional-radiative models, however, are only two-dimensional. Indeed, the glow discharge cells under investigation in our work are assumed to be cylindrically symmetrical. Hence the three dimensions can then be reduced to two dimensions (axial and radial direction). In the following, the various models will be explained in more detail.

6.2.2 MONTE CARLO MODEL FOR FAST ELECTRONS

The behavior of the fast electrons is simulated by following a large number of electrons, one after the other, during successive time steps. During each time step, the trajectory of an electron is calculated with Newton's laws:

$$\begin{aligned}
z &= z_0 + v_{z_0}\Delta t + \frac{qE_{\mathrm{ax}}(z,r,t)}{2m}(\Delta t)^2 \\
x &= x_0 + v_{x_0}\Delta t + \frac{qE_{\mathrm{rad}}(z,r,t)\cos(\alpha)}{2m}(\Delta t)^2 \\
y &= y_0 + v_{y_0}\Delta t + \frac{qE_{\mathrm{rad}}(z,r,t)\sin(\alpha)}{2m}(\Delta t)^2 \\
v_z &= v_{z_0} + \frac{qE_{\mathrm{ax}}(z,r,t)}{m}\Delta t \\
v_x &= v_{x_0} + \frac{qE_{\mathrm{rad}}(z,r,t)\cos(\alpha)}{m}\Delta t \\
v_y &= v_{y_0} + \frac{qE_{\mathrm{rad}}(z,r,t)\sin(\alpha)}{m}\Delta t
\end{aligned} \tag{6.1}$$

where z_0, x_0, y_0 and z, x, y are the position coordinates before and after Δt, v_{z_0}, v_{x_0}, v_{y_0} and v_z, v_x, v_y are the velocities before and after Δt. E_{ax} and E_{rad} are the axial and radial electric field, as a function of axial and radial position and time (obtained from the argon ion–slow electron fluid model, see below), α is the azimuthal angle of the radial position (i.e. the angle of the radial position coordinates with respect to the x-axis), and q and m are the electron charge and mass, respectively.

The probability of collision during that time step, $\mathrm{Prob}_{\mathrm{coll}}$, is calculated and compared with a random number between 0 and 1:

$$\mathrm{Prob}_{\mathrm{coll}} = 1 - \exp\{-\Delta s\,\Sigma[n\sigma_{\mathrm{coll}}(E)]\} \tag{6.2}$$

where Δs is the distance traveled during Δt and n and $\sigma_{\mathrm{coll}}(E)$ are the densities of the target particles and the cross-sections of the different collision types of the electron with energy E. If the probability is lower than the random number, no collision occurs, and the Monte Carlo solver continues with the next electron during that time step. If the probability is higher, a collision takes place. The collisions taken into account in the model are elastic collisions with argon ground-state atoms, electron impact ionization, excitation and de-excitation for all argon atom levels, copper atom and copper ion levels, as well as electron impact ionization from Ar^+ ions and two-electron impact ionization from Ar^0 to Ar^{2+}. Finally, electron–electron Coulomb scattering is also taken into account. To determine which collision takes place, the partial collision probabilities of the various collisions are calculated, and the total collision probability, which is equal to one, as it is the sum over all partial collision probabilities, is subdivided in intervals with lengths corresponding to these partial collision probabilities. A second random number between 0 and 1 is generated, and the interval in which the random number falls determines the collision that takes place. Then, the new energy and direction after collision are also defined by random numbers, based on energy and angular differential cross-sections.

This procedure is repeated for the next electron during that time step, and so on, until all electrons are followed. Then, the Monte Carlo procedure is repeated during the next time step, again for all electrons, and so on, until a steady state is reached. However, the electrons can also be removed from the Monte Carlo model, when they undergo recombination at the cell walls, or (at least in the dc discharge) when they are transferred to the slow electron group. The latter occurs when they reach energies lower than the threshold for inelastic collisions. Indeed, these 'slow' electrons are only important for carrying the electrical current and for providing negative space charge, and they can as well be described with a fluid model (see below), to save calculation time. However, when we want to calculate the detailed excitation and de-excitation between the various excited argon and copper levels for the collisional-radiative models (see below), all electrons, also the slow ones, are simulated with the Monte Carlo model, because low-energy electrons can cause de-excitation or excitation to nearby levels. More information about this model can be found elsewhere [23–27].

6.2.3 FLUID MODEL FOR ARGON IONS AND SLOW ELECTRONS

As mentioned in the Introduction, a fluid model consists generally of the (first three) velocity moments of the Boltzmann equation: continuity of particle density, of momentum density and of energy density. In our model, the energy balance equation is generally not solved, because the energy of the fast electrons and of the argon ions in the CDS is calculated with a Monte Carlo model, and the slow electrons and argon ions in the negative glow (NG) can be considered to be thermalized. Moreover, the momentum equations for argon ions and electrons are reduced to the transport equations based on diffusion and migration in the electric field. The latter is justified when the collision mean free path is much smaller than the typical cell dimensions, which is definitely the case for most analytical glow discharges, where the pressure is typically in the range 0.5–5 Torr.

As argon ionic species, Ar^+, Ar^{2+} and $Ar_2{}^+$ ions are taken into account in this model. The continuity equations and transport equations for the three types of argon ions and for the slow electrons are coupled to Poisson's equation to obtain a self-consistent electric field distribution, which is used later on in the electron and argon ion Monte Carlo models to calculate the trajectory by Newton's laws.

This yields the following equations:

$$
\begin{aligned}
\frac{\partial n_{\mathrm{Ar^+}}(z,r,t)}{\partial t} + \overline{\nabla}\cdot\overline{j_{\mathrm{Ar^+}}}(z,r,t) &= R_{\mathrm{prod,Ar^+}}(z,r,t) - R_{\mathrm{loss,Ar^+}}(z,r,t) \\
\frac{\partial n_{\mathrm{Ar^{2+}}}(z,r,t)}{\partial t} + \overline{\nabla}\cdot\overline{j_{\mathrm{Ar^{2+}}}}(z,r,t) &= R_{\mathrm{prod,Ar^{2+}}}(z,r,t) - R_{\mathrm{loss,Ar^{2+}}}(z,r,t) \\
\frac{\partial n_{\mathrm{Ar_2^+}}(z,r,t)}{\partial t} + \overline{\nabla}\cdot\overline{j_{\mathrm{Ar_2^+}}}(z,r,t) &= R_{\mathrm{prod,Ar_2^+}}(z,r,t) - R_{\mathrm{loss,Ar_2^+}}(z,r,t) \\
\frac{\partial n_{\mathrm{e,slow}}(z,r,t)}{\partial t} + \overline{\nabla}\cdot\overline{j_{\mathrm{e,slow}}}(z,r,t) &= R_{\mathrm{prod,e,slow}}(z,r,t) \\
&\quad - R_{\mathrm{loss,e,slow}}(z,r,t) \\
\overline{j_{\mathrm{Ar^+}}}(z,r,t) &= \mu_{\mathrm{Ar^+}} n_{\mathrm{Ar^+}}(z,r,t)\overline{E}(z,r,t) \\
&\quad - D_{\mathrm{Ar^+}}\overline{\nabla} n_{\mathrm{Ar^+}}(z,r,t) \\
\overline{j_{\mathrm{Ar^{2+}}}}(z,r,t) &= \mu_{\mathrm{Ar^{2+}}} n_{\mathrm{Ar^{2+}}}(z,r,t)\overline{E}(z,r,t) \\
&\quad - D_{\mathrm{Ar^{2+}}}\overline{\nabla} n_{\mathrm{Ar^{2+}}}(z,r,t) \\
\overline{j_{\mathrm{Ar_2^+}}}(z,r,t) &= \mu_{\mathrm{Ar_2^+}} n_{\mathrm{Ar_2^+}}(z,r,t)\overline{E}(z,r,t) \\
&\quad - D_{\mathrm{Ar_2^+}}\overline{\nabla} n_{\mathrm{Ar_2^+}}(z,r,t) \\
\overline{j_{\mathrm{e,slow}}}(z,r,t) &= -\mu_{\mathrm{e,slow}} n_{\mathrm{e,slow}}(z,r,t)\overline{E}(z,r,t) \\
&\quad - D_{\mathrm{e,slow}}\overline{\nabla} n_{\mathrm{e,slow}}(z,r,t) \\
[\nabla^2 V(z,r,t) + (e/\varepsilon_0)[n_{\mathrm{Ar^+}}(z,r,t) &+ n_{\mathrm{Ar^{2+}}}(z,r,t) + n_{\mathrm{Ar_2^+}}(z,r,t) - n_{\mathrm{e,slow}}(z,r,t) \\
&\quad - n_{\mathrm{e,fast}}(z,r,t)] = 0; \overline{E} = -\overline{\nabla} V]
\end{aligned}
\tag{6.3}
$$

n and j, respectively, are the densities and fluxes of the argon ionic species and electrons, R_{prod} and R_{loss} are the production and loss rates (see Table 6.2 for the reaction mechanisms). Production of Ar^+ ions is due to electron impact ionization, which is calculated in the electron Monte Carlo model above, as well as Ar^{2+}–electron recombination. Loss of Ar^+ ions is due to Ar^+–electron recombination, atomic to molecular ion conversion from Ar^+ to $\mathrm{Ar_2}^+$ and electron impact ionization from Ar^+ to Ar^{2+}. The production processes for the Ar^{2+} ions include electron impact ionization from Ar^0 and from Ar^+, as calculated in the Monte Carlo model above. The loss processes are Ar^{2+}–electron recombination and two-electron asymmetric charge transfer with Cu^0, being a resonant process [28]. Production of $\mathrm{Ar_2}^+$ ions is caused by associative ionization of argon atoms (Hornbeck–Molnar process or due to the collision of two argon metastable atoms), as well as by atomic ion to molecular ion conversion (see above). Loss of $\mathrm{Ar_2}^+$ ions is assumed to occur entirely due to dissociative recombination. Finally, production of the slow electrons is due to electron transfer to the slow electron group (calculated in the above electron Monte Carlo model), whereas loss of these electrons is due to various electron–argon ion recombination mechanisms. Further, $\overline{E}$ is the electric field and V is the electric potential. D and μ, respectively, are the diffusion coefficients and mobilities of the argon ionic species and electrons.

The four transport equations can be inserted into the four continuity equations, leading to a set of five coupled differential equations, including Poisson's equation, with boundary conditions: $V = -V_c$ at the cathode [or $V(t) = V_{dc} + V_{rf}\sin(\omega_{rf}t)$ in the rf discharge, where V_{dc} is the dc bias voltage, V_{rf} is the applied rf voltage and ω_{rf} is the rf frequency] and $V = 0$ at the anode; $n_{e,slow} = 0$ at all walls and all times because electron–ion recombination at a conducting surface is assumed to be infinitely fast, and $\overline{\nabla} n_{Ar^+}, \overline{\nabla} n_{Ar^{2+}}, \overline{\nabla} n_{Ar_2{}^+} = 0$ at all walls and all times. The latter means that the ion fluxes at the walls are only due to migration. This forces a nonzero ion density at the electrodes, although it is expected that the ion density is zero or close to zero, owing to Auger neutralization. Hence this boundary condition is not completely correct, but it is used to avoid numerical difficulties due to a very thin ion diffusion boundary layer.

Owing to the severe nonlinearity and strong coupling of the equations, solving this model is a difficult numerical problem. The method we used was developed by Passchier and Goedheer [4], and is based on the Scharfetter–Gummel exponential scheme for the transport equations [29,30]. The basic idea is that the particle fluxes are assumed constant between mesh points, instead of the densities. The advantage of this scheme is its ability to switch between situations where either the migration component or the diffusion component of the particle flux is dominant, namely in the high and low electric field, sheath region (CDS) and bulk plasma (NG), respectively. More details about this model can be found in the literature [24–27,31,32].

6.2.4 MONTE CARLO MODEL FOR ARGON IONS AND FAST ARGON ATOMS IN THE CDS

As mentioned before, the argon ions are not really in equilibrium with the strong electric field in the CDS, and the fluid model is, therefore, only an approximation for the argon ions in this region. Therefore, the argon ions are also simulated with a Monte Carlo method in this region, which enables us to calculate the argon ion energy distribution at the cathode, needed to calculate the amount of sputtering (see below). Only the Ar^+ ions are treated with this Monte Carlo model, because the Ar^{2+} and $Ar_2{}^+$ ions have a lower density and flux, and they play only a minor role in the sputtering process [32]. However, in addition to the Ar^+ ions, also the fast argon atoms (Ar_f^0), which are created by collisions of the argon ions, are described with this Monte Carlo model, since it was found that they play a dominant role in the sputtering process [23].

The argon ion and fast argon atom Monte Carlo model is similar to the electron Monte Carlo model. Indeed, during successive time steps, the trajectory of the ions and atoms is calculated by Newton's laws, and the occurrence of a collision, the nature of the collision and the new energy and direction after collision are determined by random numbers. The collision processes taken into account are elastic scattering collisions with argon ground-state atoms, for both ions and atoms, symmetric charge transfer for argon ions (which is actually also a form of elastic collisions, because there is no change in kinetic energy), and ion and atom impact ionization, excitation and de-excitation for all argon atom levels.

The ions are followed until they bombard the cathode. Then, the 'fast' (i.e. nonthermal) argon atoms created by collisions of the ions, are also followed, until they collide at the walls or until they are again thermalized by collisions. More information about this Monte Carlo model can be found in the literature [23,33,34].

6.2.5 HEAT TRANSFER MODEL FOR ARGON GAS ATOMS

In most cases, we have assumed in our model that the argon gas atoms are at rest, uniformly distributed throughout the discharge, and that no specific model is applied to describe their behavior. However, recently we have developed a model for the dc discharge to calculate gas heating, and consequently the gas temperature distribution, which yields, when the gas pressure is constant, a nonuniform gas density distribution. The gas temperature is calculated as a function of z and r position with the heat conduction equation:

$$\frac{\partial^2 T_g}{\partial z^2} + \frac{1}{r}\frac{\partial}{\partial r}\left(r\frac{\partial T_g}{\partial r}\right) = -\frac{P}{\kappa} \tag{6.4}$$

where T_g is the argon gas temperature, P is the power input and κ is the thermal conductivity ($= 1.8 \times 10^{-4}\ \mathrm{W\,cm^{-1}\,K^{-1}}$ for argon). The power input in the argon gas is calculated in the ion and atom Monte Carlo models, based on collisions and subsequent energy transfer of the argon ions, fast argon atoms and copper atoms (see below) to the argon gas atoms. A detailed description of this model can be found in Bogaerts *et al.* [35].

6.2.6 COLLISIONAL-RADIATIVE MODEL FOR ARGON ATOM EXCITED LEVELS

Figure 6.1 shows a schematic energy diagram of the argon atomic levels taken into account in our model. Sixty-four argon atomic excited levels are considered; most of them are effective levels, i.e. a group of individual levels with comparable excitation energy and quantum numbers. The four 4s levels, being two metastable levels and two resonant levels, are, however, treated separately. The behavior of these levels is described with 64 coupled balance equations,

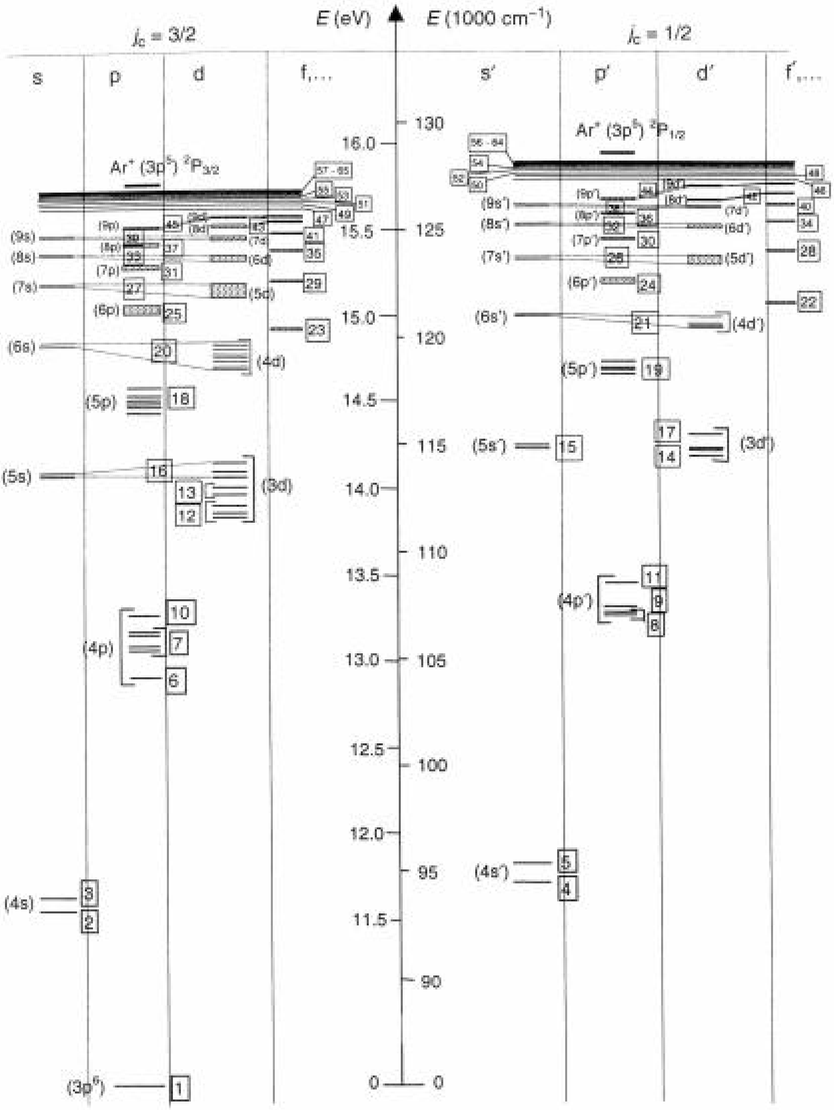

Figure 6.1 Argon atom energy level scheme, illustrating all the effective levels incorporated in the model. Reproduced by permission of The American Institute of Physics from Bogaerts, A., Gijbels, R., and Vlcek, J., *J. Appl. Phys.* 1998, **84**, 121–136

taking into account a large number of populating and depopulating collisional and radiative processes:

$$\frac{\partial n_{\mathrm{Ar}^*}(z,r,t)}{\partial t} - D_{\mathrm{Ar}^*}\frac{1}{r}\frac{\partial}{\partial r}\left[r\frac{\partial n_{\mathrm{Ar}^*}(z,r,t)}{\partial r}\right] - D_{\mathrm{Ar}^*}\frac{\partial^2 n_{\mathrm{Ar}^*}(z,r,t)}{\partial z^2}$$
$$= R_{\mathrm{prod}}(z,r,t) - R_{\mathrm{loss}}(z,r,t) \tag{6.5}$$

The production and loss processes taken into account are electron, argon ion and atom impact ionization from all levels, excitation and de-excitation between all these levels, and electron–ion three-body and radiative recombination to all levels, in addition to radiative decay between the levels and Hornbeck–Molnar associative ionization (for Ar^* levels with excitation energy above 14.7 eV). Moreover, some additional processes are incorporated for the 4s metastable levels, namely metastable atom–metastable atom collisions, Penning ionization of the sputtered copper atoms, and two-body and three-body collisions with argon ground state atoms (see Table 6.2 for the reaction mechanisms).

Transport occurs by diffusion; the latter plays only a role for the 4s levels, because the higher excited levels decay more rapidly to the ground state by emission of radiation than they could move due to diffusion. Furthermore, when the two non-metastable 4s levels decay to the ground state, a large fraction of the emitted radiation is re-absorbed by the ground level, leading again to formation of this 4s level. This phenomenon of 'radiation trapping' is accounted for by means of 'escape factors' which express the fraction of photons which can really escape without being re-absorbed [36,37].

The 64 balance equations are coupled to each other, because higher and lower levels affect each other owing to radiative decay, excitation and de-excitation. The boundary conditions for these equations are $n_{\mathrm{Ar}^*} = 0$ at all walls, because the excited levels will de-excite upon collision at the walls. More information about this model can be found elsewhere [38,39].

6.2.7 SPUTTERING AT THE CATHODE AND THERMALIZATION OF THE SPUTTERED ATOMS

The flux of sputtered copper atoms is calculated from the flux energy distribution functions of the argon ions, fast argon atoms and copper ions (see below) bombarding the cathode, $f(0,r,t,E)$, calculated in the Monte Carlo models. It is multiplied with an empirical equation for the sputtering yield as a function of the bombarding energy (Y), adopted from Matsunami *et al.* [40]:

$$J_{\mathrm{sput}}(0,r,t) = -\int_E \{Y_{\mathrm{Ar-Cu}}(E)[f_{\mathrm{Ar}^+}(0,r,t,E) + f_{\mathrm{Ar}_f^0}(0,r,t,E)]$$
$$+ Y_{\mathrm{Cu-Cu}}(E) f_{\mathrm{Cu}^+}(0,r,t,E)\}\,\mathrm{d}E \tag{6.6}$$

When the copper atoms are sputtered from the cathode, they have energies of the order of 5–10 eV. However, they lose these energies almost immediately in the first few millimeters from the cathode, by collisions with argon gas atoms, until they are thermalized. This thermalization process is described with a Monte Carlo model, similar to the electron Monte Carlo model (see above), except that the electric field does not come into play for the neutral atoms, and that only elastic collisions with argon atoms are incorporated. Indeed, collisions with other plasma species can be neglected, owing to the lower densities of these species. This Monte Carlo model is employed until all atoms are thermalized, and it results in a so-called thermalization profile, F_T, i.e. the number of atoms thermalized as a function of position from the cathode. More details can be found elsewhere [41].

The product of J_{sput} and F_T will be used as source term for the copper atoms, described in the next model.

6.2.8 COLLISIONAL-RADIATIVE MODEL FOR THE COPPER ATOMS AND IONS

The further behavior of the thermalized sputtered copper atoms (i.e. transport, ionization and excitation) and the behavior of the excited copper atoms and of the copper ions, both in the ground state and in excited levels, are described with a collisional-radiative model. Eight copper atom levels, seven copper ion (Cu^+) levels and the Cu^{2+} ions are considered (see the energy level scheme in Figure 6.2). Some of the Cu atom and ion levels are grouped into effective levels. The behavior of all the levels is again described with a set of coupled balance equations with various production and loss terms, i.e. electron impact ionization from all levels, excitation and de-excitation between all levels, radiative decay between all levels, electron–ion three-body recombination to the upper copper atom and copper ion levels, Penning ionization by argon metastable atoms, and asymmetric charge transfer between copper atoms and argon ions (see Table 6.2). Moreover, an additional production term for the copper ground-state atoms is the product of J_{sput} and F_T, as is described above.

The transport occurs by diffusion for the atoms, and by diffusion and migration for the ions. The equations are also coupled owing to the effect of higher and lower levels on the other levels, and they are solved until a steady state is reached. More information about this model is available [42,43].

6.2.9 MONTE CARLO MODEL FOR COPPER IONS IN THE CDS

As mentioned before, the copper ions are also treated with a Monte Carlo model in the CDS, because they are not in equilibrium with the strong electric field in this region. The procedure is again comparable to the electron Monte Carlo model,

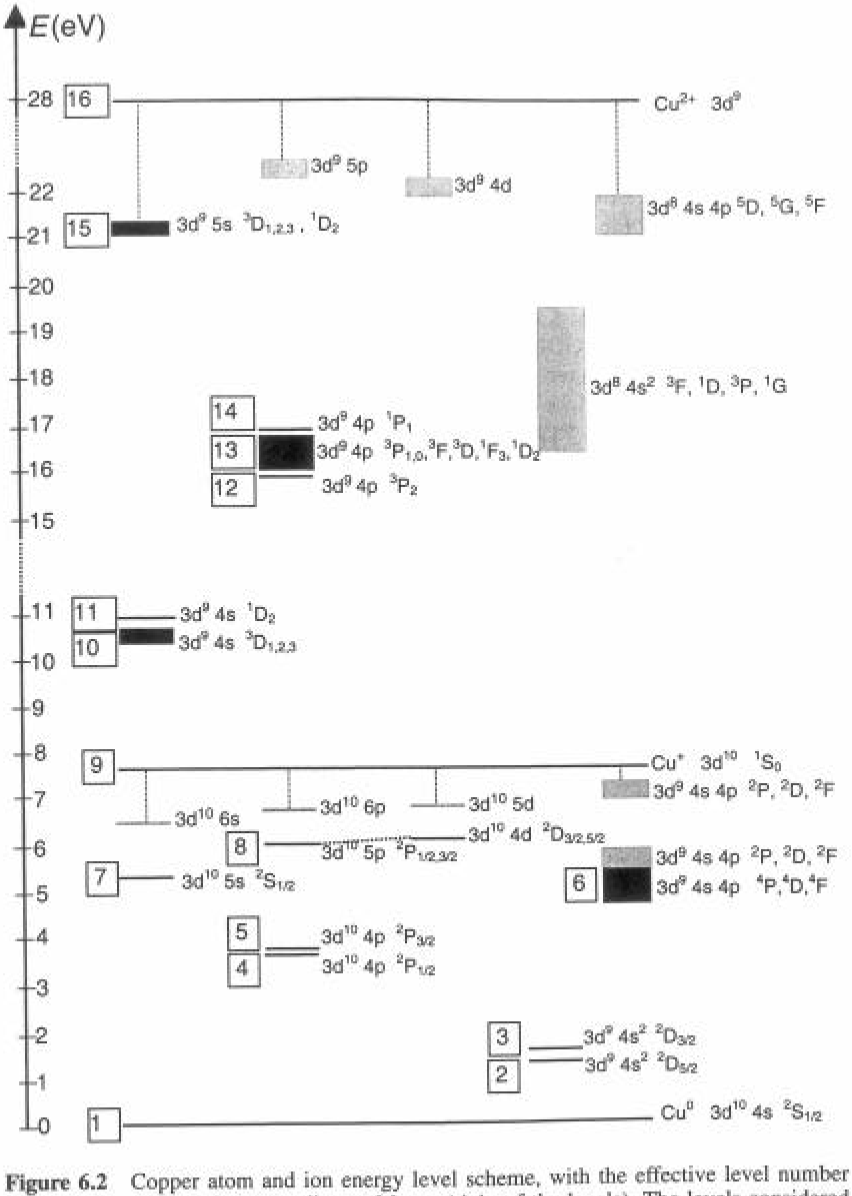

Figure 6.2 Copper atom and ion energy level scheme, with the effective level number (left) and the designation according to Moore (right of the levels). The levels considered in the model are presented in black. Reprinted from Bogaerts, A., Gijbels, R., and Carman, R. J., *Spectrochim. Acta, Part B*, 1998, **53**, 1679–1703, with permission of Elsevier Science

and includes calculation of the trajectory by Newton's laws, and treatment of the collisions by random numbers (for more information, see earlier papers [44,45]).

6.3 RESULTS AND DISCUSSION

An overview of the typical quantities that have been calculated with our models is given in Table 6.4. Comparison is made with experimental data, when available. More details about the calculation results and the comparison with experiments can be found in the references mentioned. In the following, some of the calculation results will be discussed in more detail, to illustrate the possibilities and limitations of our models. Calculations have mainly been performed for dc glow discharges, under both GDMS and GD-OES (Grimm-type) conditions; therefore, most results presented below apply to dc glow discharges. Nevertheless,

Table 6.4 Overview of the typical results obtained with our models, and comparison with experimental data, if available.

Calculated quantities (+ ref. for more information)		Comparison with experimental data (+ ref.)	
Electrical characteristics:			
Current as a function of voltage and pressure (dc)	[33,46,47]	Measured for VG 9000 cell	[33,46]
Rf amplitude and dc bias voltage (rf)	[31,48,49]	Measured for Grimm-type cell	[49]
Voltage, current, power as a function of time (μs-pulsed)	[27]	Measured for Grimm-type cell	[50]
Potential, electric field distributions:			
3D potential distributions	[24–27,31,46]	—	
3D axial and radial electric field distributions	[24–27,31,46]	—	
Value of the plasma potential	[24–27,31,46]	—	
Lengths of the different regions (CDS, NG)	[24–27,31,46]	Length of CDS as function of pressure and current: empirical equation of Aston	[46,51]
3D density profiles of:			
Argon atoms (gas heating)	[35]	—	
Argon ions	[24–27,31,46]	—	
Fast argon atoms	[23,46]	—	
Argon metastable atoms	[38,39,45,46,52]	Measured (for dc discharge) by laser induced fluorescence (LIF)	[53]

Table 6.4 (*continued*)

Calculated quantities (+ ref.for more information)		Comparison with experimental data (+ ref.)	
Other argon excited levels	[38,39]	—	
Fast electrons	[23–25,46]	—	
Thermalized electrons	[24–27,31,46]	Measured by Langmuir probe (dc)	[54]
Atoms of the cathode material	[42–46]	Measured by LIF (dc)	[55]
Ions of the cathode material	[42–46]	Measured by LIF (dc)	[55]
Atoms + ions of the cathode material, in excited levels	[42,43]		
Ion fluxes of argon and cathode ions at the exit slit of the cell to the mass spectrometer (dc)	[56,57]	Ratio in qualitative agreement with ratios in dc GD mass spectra	[56]
Ionization degrees of argon and cathode atoms	[44–46]	Based on the LIF results (see above)	[55]
3D energy distributions and mean energies of:			
Electrons	[22,24,26,31,46]	—	
Argon ions	[22,34,46]	Measured at cathode for dc GDMS	[58]
Fast argon atoms	[23,34,46]	—	
Cathode ions	[44,46]	Measured at cathode for dc GDMS	[58]
Information about collision processes:			
3D collision rates of the different collision processes of electrons, argon ions and fast argon atoms and relative importances of these collision processes	[23–27,31,33,46]	—	
3D rates of Penning ionization, asymmetric charge transfer and electron impact ionization and relative contributions to the total ionization of sputtered atoms	[42–46]	—	

(*continued overleaf*)

Table 6.4 (*continued*)

Calculated quantities (+ ref. for more information)		Comparison with experimental data (+ ref.)	
3D rates and relative contributions of the various populating and depopulating processes (see text) of the metastable and other excited argon levels	[38,39,45,46,52]	—	
3D rates and relative contributions of the various populating and depopulating processes (see text) of the excited cathode atom + ion levels	[42,43]	—	
Information about sputtering:			
Sputtering (erosion) rates at the cathode	[43–47,59]	Values for GDMS, GD-OES, dc, rf	[49,60–62]
Thermalization profiles of the sputtered atoms	[41,46]	—	
Amount of redeposition on the cathode by backscattering or back-diffusion	[41,46,59]	—	
Relative contributions of argon ions, fast argon atoms and cathode ions to the sputtering process	[23,43–46]	—	
2D crater profiles due to sputtering at the cathode	[59]	Profiles obtained for GDMS	[60]
Emission spectra and emission spatial distributions due to radiative decay from the excited levels (for argon and cathode atoms + ions)	[39,43,63–65]	Data from the literature	[66–68]
Effect of cell geometry on the calculated quantities	[56,57]	—	
Prediction of variations in relative sensitivity factors for GDMS	[69]	Data from the literature	[17]

calculations have also been carried out for rf and microsecond-pulsed discharges, and some of these results will also be discussed below.

6.3.1 ELECTRICAL CHARACTERISTICS

The only input parameters in the model are the cell geometry, the kind of discharge gas and the corresponding cross-sections, and also in general the discharge voltage, gas pressure and gas temperature. The electric current, which is another macroscopic quantity, follows self-consistently from the calculation results, as the sum of the microscopic fluxes of charged plasma species. Since this parameter is, hence, one of the final results of the model, as it is summed over the various charged species, and since it is also experimentally available, it can be used to check the validity of the model. Indeed, when a realistic value for this calculated current is obtained, it can be expected that the other calculated microscopic plasma quantities (fluxes, densities, etc.) are also more or less realistic.

Figure 6.3 presents the calculated dc electrical current as a function of voltage and pressure, for the VG 9000 glow discharge cell (Thermo Elemental; solid lines, left axis). Current–pressure–voltage characteristics were also measured for the same cell, and the results are also included in Figure 6.3 (dashed lines, right axis). The agreement between theory and experiment is reasonable, in so far that the current increases in a similar way with pressure and voltage. Indeed, at higher pressures, there are more gas atoms, and therefore more ionization collisions and hence the creation of more ions and electrons, which means that more current will

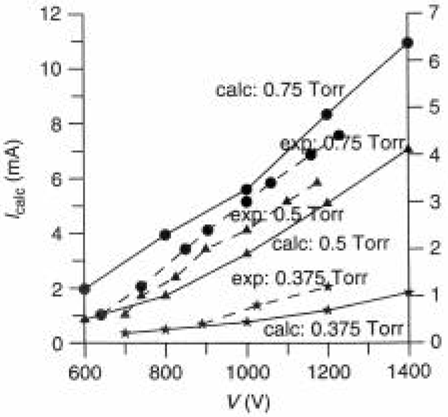

Figure 6.3 Electrical current as a function of voltage at three pressures in a dc discharge (standard VG 9000 flat cell). The calculation results are presented by the solid lines (left axis), whereas the experimental values [72] are shown with dashed lines (right axis; note the different vertical scale)

flow through the discharge cell. The effect of the voltage is explained as follows. At low voltages (below 600 V), the electrons have low energies (below the maximum in the electron impact ionization cross-section, at ca 100 eV) [70], and increasing the voltage means that the electrons will reach more suitable energies for ionization, leading to more electrons and ions, hence yielding a higher current. At voltages above 600 V, the electrons have too high energies for efficient ionization, and increasing the voltage means that the amount of electron impact ionization will decrease again. However, at these high voltages, other processes such as argon ion and atom impact ionization come into play. The cross-sections of these processes reach their maximum at much higher energies (1000 eV and more) [71], allowing a further increase in current with rising voltage. Indeed, in the model described by Bogaerts *et al.* in 1995 [24], argon ion and atom impact ionization were not yet incorporated, and the correct current–voltage behavior could therefore not yet be predicted.

Exact quantitative agreement between the experimental and calculated current–voltage relations is, however, not yet reached (note the different scales on the y-axis), and can, in fact, at present not yet be expected. Indeed, the pressure can in principle not directly be measured in the VG 9000 glow discharge cell. In order to obtain current–voltage characteristics at specific pressures, the pressure was measured with a thermocouple [72], but these measured pressures in Figure 6.3 are subject to uncertainties. More recently, Venzago and co-workers have proposed a pressure measurement in the VG 9000 cell, with the aid of a Baratron capacitance manometer, which might be more reliable [73]. Moreover, the exact gas temperature in the discharge cell is not known. We assumed a gas temperature of 300–380 K (rising with pressure and voltage), because this is a reasonable value, in so far as it is expected that the gas temperature in the discharge is higher than room temperature at the present conditions, and it yields realistic current values. For the sake of simplicity, we assumed uniform values throughout the discharge. However, our gas heating calculations [35] predict some temperature gradients in the discharge (see below). Since small variations in the gas temperature had already a significant effect on the electrical current (e.g. 30% variation in gas temperature yields a change in electrical current by as much as 100%) [46], the quantitative results of the model have to be considered with caution.

Since the gas temperature is such a critical input parameter, we have tried to calculate this value for a dc glow discharge with the heat transfer equation. The resulting two-dimensional distributions, both for the VG 9000 GDMS cell and a Grimm-type cell, are presented in Figure 6.4, for typical dc GDMS and GD-OES operating conditions. The cathode is found at the left end of both parts of the figure, whereas the other borders of the figure represent the anode cell walls (grounded). The black rectangles in Fig. 6.4a symbolize the insulating ring (from $z = 0$ to 0.05 cm) and anode front plate (from $z = 0.05$ to 0.15 cm). In Figure 6.4b, not the entire Grimm cell geometry, but only the first 1.5 cm from

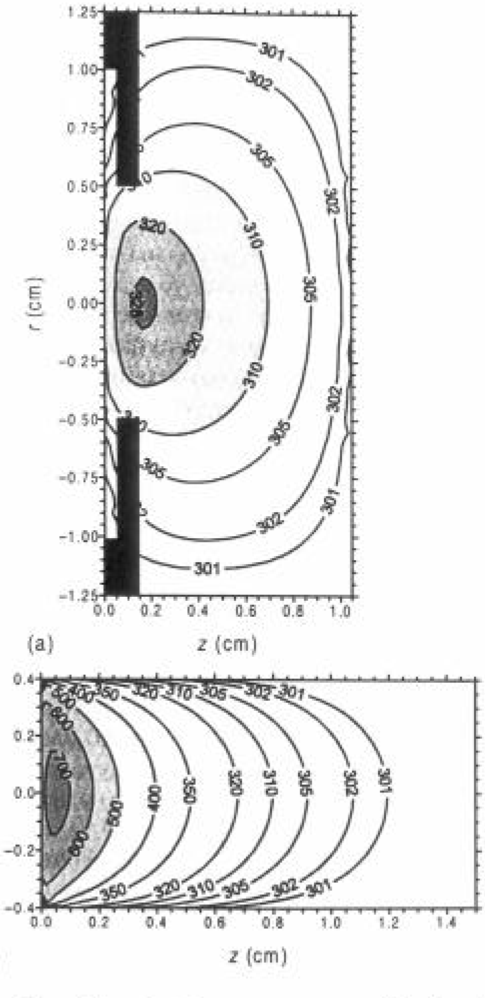

Figure 6.4 Calculated two-dimensional gas temperature profiles in a dc discharge, (a) in the VG 9000 cell at 1000 V, 0.5 Torr and 3.5 mA and (b) in a Grimm-type cell at 800 V, 3 Torr and 52 mA. The cathode is found at the left end of both parts, whereas the other borders of the figures represent the anode cell walls (grounded). The black rectangles in (a) symbolize the insulating ring (from $z = 0$ to 0.05 cm) and anode front plate (from $z = 0.05$ to 0.15 cm). In (b), not the entire cell geometry but only the first 1.5 cm from the cathode is shown, because the gas heating was found to be negligible at larger distances from the cathode. Reproduced by permission of the American Institute of Physics from Bogaerts, A., Gijbels, R., and Serikov, V. V., *J. Appl. Phys.*, 2000, **87**, 8334–8344

the cathode is shown, because the gas heating was found to be negligible at larger distances away from the cathode. It is clear that the temperature in the VG 9000 cell rises only moderately, whereas a considerable increase in gas temperature was computed for the Grimm-type cell. The reason is, of course, that the Grimm-type cell is operated at much higher electrical powers, yielding a much higher power input into the argon gas. It should be mentioned, however, that the calculated gas temperatures are still subject to considerable uncertainties, owing to some input parameters in the heat transfer equation which are unknown, such as the thermal accommodation coefficient at the cell walls, and the cathode temperature. The latter affects the calculated gas temperature to a large extent. Hence this seems to shift the problem of unknown gas temperature to the problem of unknown cathode temperature. The situation might be further complicated when the glow discharge cell is cooled with liquid nitrogen, as is the case with the VG 9000 cell. Nevertheless, the spatial distributions of the calculated gas temperatures, and also their qualitative rise with respect to the cathode temperature, are expected to be fairly realistic.

The importance of the gas temperature as input in the model has also been demonstrated [27] for a microsecond-pulsed glow discharge. Indeed, it was found that when the gas temperature was assumed to be constant in time, the model could not predict the experimental electrical current and power behavior as a function of time in the microsecond-pulsed discharge. Figure 6.5 shows the applied voltage, and also the resulting electrical current and power, and the gas temperature assumed in the model, as a function of time during and after the pulse. The values used as input (i.e. voltage and gas temperature) or calculated (i.e. current and power) in the model are represented by the solid lines, whereas the experimental data are plotted with dashed lines. The gas pressure was measured to be 3 Torr and assumed to be constant in time. A voltage of 1500–2000 V is applied during 10 μs, and then it drops exponentially, reaching zero at about 40 μs after initiation of the pulse (see Figure 6.5a). The electrical current (Figure 6.5b), and hence also the power (Fig. 6.5c), appear to rise significantly to values of almost 1 A and 1.5 kW, respectively, at 1.5–2 μs, and then they drop almost as rapidly to 'plateau values' of about 100 mA and 200 W, respectively, which are more or less maintained from 4 to 10 μs. After the pulse, the current and power decay to zero at about 20 μs after the start of the pulse. This experimental behavior of current and power could only be predicted with our model if a time-varying gas temperature (see Figure 6.5d) was assumed. Indeed, at the start of the pulse, the gas is at room temperature. However, the gas temperature will increase rapidly as a function of time, owing to the high electrical power, and hence high power input into the argon gas. When the power has dropped to a plateau value of ca 200 W, the gas temperature will not increase further, but on the other hand, the power is still high enough to maintain the high gas temperature. Only when the power has dropped further, after the pulse, does the gas temperature decrease exponentially. It was found to reach room temperature again around 200 μs [27],

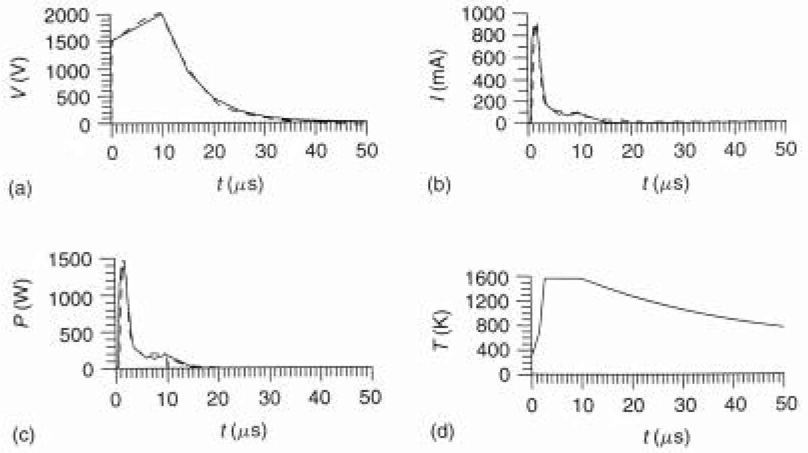

Figure 6.5 Calculated electrical characteristics as a function of time during and after the pulse, in a microsecond-pulsed glow discharge at a gas pressure of 3 Torr, an applied voltage of 2 kV, a pulse width of 10 μs and a pulse repetition frequency of 200 Hz. The data used as input or calculated in the model are represented by solid lines: (a) applied voltage assumed in the model; (b) calculated electrical current; (c) calculated electrical power; (d) gas temperature assumed in the model. The experimental data in (a)–(c) are plotted with dashed lines

hence well before the next pulse will be applied, at the pulse repetition frequency of 200 Hz used in the experiment. The time evolution of the gas temperature presented in Figure 6.5d was used as a kind of fitting parameter in our model, to obtain reasonable agreement with the experimental behavior of voltage, current and power as a function of time. Nevertheless, the assumed values have also been checked, at least qualitatively, with a time-dependent heat transfer equation, and it was illustrated that the fitted time evolution of the gas temperature was indeed realistic [27].

In our model for rf glow discharges, not the voltage but the power is used as an input value in addition to the gas pressure and temperature. The applied voltage at the rf electrode and the dc bias voltage are then calculated, based on the conditions that (i) the power dissipated by electrons and ions in the discharge should be equal to the applied rf power, (ii) the product of rf voltage and current, averaged over time, should be equal to the applied rf power and (iii) the total current towards the rf electrode, integrated over one rf cycle, should be zero, as it is imposed by the capacitive coupling of both electrodes. Figure 6.6a shows the calculated voltage at the rf electrode as a function of time in the rf cycle (thick solid line), at an electrical power of 37 W and a gas pressure of 5 Torr. The voltage is negative during most of the rf-cycle, except around $\omega t = \pi/2$. This is attributed to the highly negative dc bias voltage of −519 V (see thin

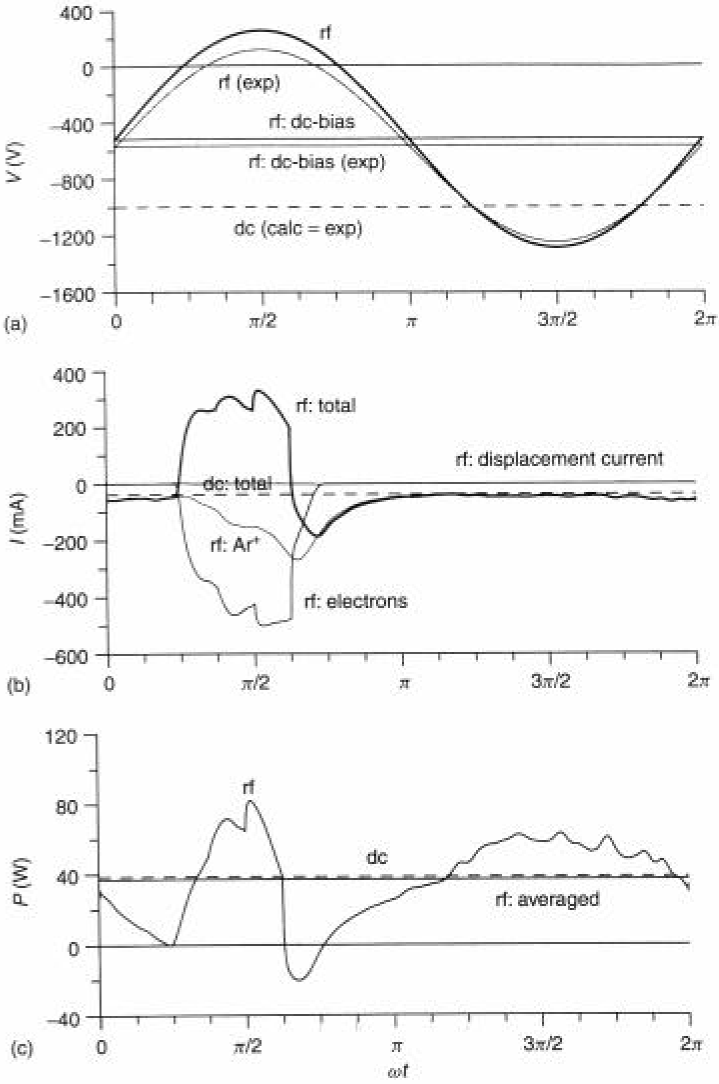

Figure 6.6 Calculated electrical characteristics as a function of time in the rf cycle, in the rf discharge (solid lines) and in a dc discharge (constant in time; dashed lines), at a gas pressure of 3 Torr and an electrical power of 37–38 W. (a) Voltage (the experimental values are also presented, in gray lines); (b) current, including the contributions of ion and electron current and displacement current at the rf electrode, in the rf case (in thinner lines); (c) electrical power. Reprinted from Bogaerts, A., and Gijbels, R., *Spectrochim. Acta, Part B*, 2000, **55**, 263–278, with permission of Elsevier Science

solid line), which arises from the large difference in size between the rf-powered and grounded electrode, in combination with the capacitive coupling of both electrodes. The experimental rf voltage as a function of time and the experimental dc bias voltage are also illustrated in Figure 6.6a (gray lines) [49]. It appears that our calculated amplitude for the rf voltage was slightly too high and our dc bias voltage was too low, but in general, the agreement with experiments was considered satisfactory. The voltage obtained in the dc case, for the same values of power and pressure, is also presented in Figure 6.6a (dashed line). There was excellent agreement with the experimental value, as demonstrated in the figure.

The electrical current flowing towards the rf electrode is plotted against time in the rf cycle in Figure 6.6b (thick solid line), together with the individual contributions of electron and argon ion currents and the rf displacement current at the rf electrode. The latter arises from the moving of the rf sheath as a function of time, which gives rise to a variation of charge in the sheath as a function of time, and hence to an electrical current (since $I = \mathrm{d}q/\mathrm{d}t$, where I is the current, q is the charge and t is the time). It appears that for the conditions under study here, the displacement current makes only a minor contribution to the total current, as is expected since the rf sheath does not move considerably with time owing to the large dc bias voltage. It should be mentioned, however, that the displacement current can play a dominant role in rf discharges used for technological applications [74,75], which are mostly characterized by two electrodes of similar size and which operate at lower pressures. It is clear from Figure 6.6b that the total electrical current at the rf electrode is mainly due to argon ions. Only around $\omega t = \pi/2$, where the rf voltage is positive, is a large electron current observed at the rf electrode. It contributes to the total current with an opposite sign, so that the total current to the rf electrode, integrated over the rf cycle, is equal to zero, as is imposed by the capacitive rf coupling. The current in the dc discharge, under the same conditions of power and pressure, is also presented in Figure 6.6b (dashed line; constant in time). It is slightly lower than the rf current, which is of course necessary when the voltage is higher and the electrical power is the same.

The product of voltage and current gives rise to the electrical power, which is presented as a function of time in Figure 6.6c. The time-averaged value is also illustrated, in addition to the dc value (dashed line; constant in time). The fact that these values are equal to the input values in the model illustrates that the time evolution of voltage and current is correctly calculated in our model.

6.3.2 POTENTIAL AND ELECTRIC FIELD DISTRIBUTIONS

As mentioned before, the model is completely self-consistent, i.e. the potential and the electric field distributions used to calculate the trajectories of the charged plasma species in the Monte Carlo models are in their turn obtained from the calculated densities of these plasma species, via Poisson's equation in the slow electron–argon ion fluid model.

In Figure 6.7, the two-dimensional potential distribution is illustrated for a dc discharge, calculated for the VG 9000 cell at 1000 V, 0.5 Torr argon gas pressure and 3.5 mA current. The potential is equal to −1000 V at the cathode and increases very rapidly towards zero at about 0.24 cm from the cathode. This position where the potential crosses zero is defined as the interface between cathode dark space (CDS) and negative glow (NG). In the NG, the potential is slightly positive (approximately 10 V for these discharge conditions and cell geometry). This value is called the 'plasma potential'. It drops again to zero at the anode walls, which are grounded. The value of the plasma potential does not depend

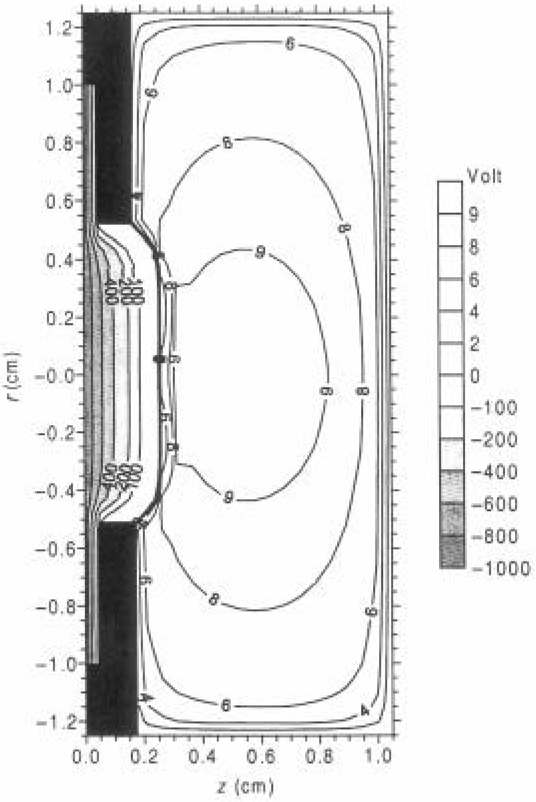

Figure 6.7 Calculated two-dimensional potential distribution in a dc discharge, in the VG 9000 cell at 1000 V, 0.5 Torr and 3.5 mA. Reprinted with permission from Bogaerts, A., Gijbels, R., and Goedheer, W. J., *Anal. Chem.*, 1996, **68**, 2296–2303, Copyright 1996 American Chemical Society

strongly on the discharge conditions, but it varies with the cell dimensions, ranging from about 1 V in large cells (diameter of a few centimeters) [56] to several tens of volts in small cells (diameter of a few millimeters) [47]. The length of the CDS, on the other hand, does not depend on the cell dimensions, but it varies strongly with the discharge conditions [33,46,47]. It rises with decreasing voltage and more significantly with decreasing pressure, ranging from about 0.5 mm at 5.25 Torr [47] to almost 8 mm at 0.375 Torr [33].

The electric field distribution can easily be derived from the potential distribution, by taking the spatial gradient. This leads to a strongly negative electric field in the CDS, which is responsible for the significant energy gain of electrons and ions in this region. In the NG, a weak electric field, both positive and negative, depending on the position, is found.

The potential and electric field distributions in the rf- and in the microsecond-pulsed discharge were calculated to be very similar to the dc potential distributions. They are characterized by a strongly negative value at the cathode (or rf electrode), a steep drop to zero in the CDS (or rf sheath) and a nearly constant, slightly positive value in the NG (or bulk plasma) [26,27,31]. Only the potential distribution around $\omega t = \pi/2$ in the rf discharge is significantly different [26,31]. This means that the potential is clearly positive at the rf electrode and has a value of about 250 V (see Figure 6.6a). It drops gradually to zero at the grounded cell walls. This gives rise to a considerable electric field in the bulk plasma around this time.

6.3.3 DENSITIES AND LEVEL POPULATIONS OF THE PLASMA SPECIES

Figure 6.8 presents the two-dimensional argon ion density profiles, for Ar^+, Ar^{2+} and $Ar_2{}^+$ ions, in the dc case, at the same discharge conditions and cell geometry as in Figure 6.7 [32]. For all three ionic species, the densities are low and fairly constant in the CDS, but they increase rapidly in the NG and reach a maximum at about 5 mm from the cathode. They decrease again to low values at the anode walls. Comparing the absolute values in the three figures tells us that the Ar^{2+}/Ar^+ and $Ar_2{}^+/Ar^+$ ratios are of the order of a few percent. This appeared to be the case for all discharge conditions investigated [32]. Moreover, the ratios of the fluxes of these ionic species at the anode backwall, where the exit slit is located in the cell of the VG 9000 mass spectrometer, were also found to be of the order of 1–10%. This is in reasonable agreement with measured intensity ratios in the glow discharge mass spectrum for Ar^{2+}/Ar^+ and $Ar_2{}^+/Ar^+$, as shown in Figure 6.9 [76].

The density of slow electrons (not shown here) is characterized by nearly the same profile as the Ar^+ ion density profile, except that it is zero in the CDS. This gives rise to a positive space charge in the CDS and nearly charge neutrality in the NG, which results in the typical potential distribution shown in Figure 6.7.

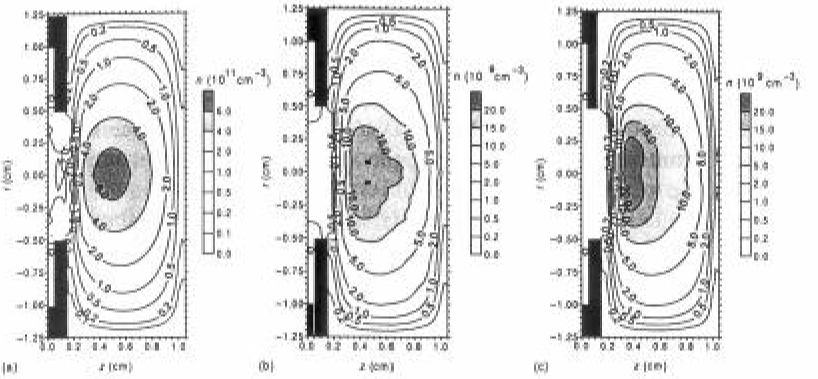

Figure 6.8 Calculated two-dimensional density profiles of the (a) Ar^+, (b) Ar^{2+} and (c) Ar_2^+ ions in a dc discharge, in the VG 9000 cell at 1000 V, 0.5 Torr and 3.5 mA. Reproduced by permission of the American Institute of Physics from Bogaerts, A., and Gijbels, R., *J. Appl. Phys.*, 1995, **78**, 6427–6431

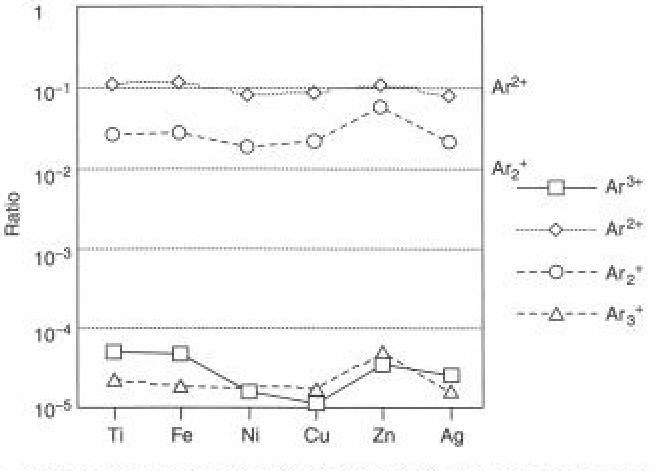

Figure 6.9 Measured intensity ratios in the VG 9000 glow discharge mass spectrum (dc discharge), for different Ar ionic species relative to Ar^+ ions, for different cathode materials [76]. Reproduced by permission of the American Institute of Physics from Bogaerts, A., and Gijbels, R., *J. Appl. Phys.*, 1995, **78**, 6427–6431

To check our calculation results for the electron densities, we performed Langmuir probe measurements in a dc Grimm-type glow discharge, under typical GD-OES discharge conditions [54]. It should be mentioned that the argon ion densities presented in Figure 6.8 were obtained at typical GDMS conditions, and that GD-OES operates generally at clearly higher pressures and currents than GDMS, namely 3–7 Torr compared with ca 1 Torr gas, and 10–50 mA compared with 1–10 mA electrical current. Hence higher electron densities are therefore expected at the GD-OES conditions. In Figure 6.10, the electron densities, calculated for the Grimm-type glow discharge, and taken at the maximum of their profile (solid lines, left axis), are compared with the experimental values for the same cell (dashed lines, right axis). The results are in satisfactory agreement, in so far as both calculated and experimental values rise to nearly the same extent with voltage and pressure. Quantitatively, we found a factor of about two difference (note the different scales on the *y*-axes). This is, however, still reasonable because it is well below the expected errors of both the model calculations (e.g. uncertainties in input data, such as gas pressure and temperature and collision cross-sections; small variations in these input data can yield significant variations in the calculation results) and the experimental data (e.g. possible disturbance of the plasma by the Langmuir probe, possible contamination due to deposition on this probe, approximations in the Langmuir probe theory).

Figure 6.11a shows the calculated two-dimensional density profile of the sputtered cathode atoms in the case of tantalum (the reason for taking tantalum as an example is given below), for a six-way cross glow discharge cell (approximated to be cylindrically symmetrical) and dc conditions of 1000 V, 1 Torr and ca 2 mA [55]. The cathode is found at the left-hand side of the figure, whereas the other borders of the figure are anode walls. The tantalum atom density reaches

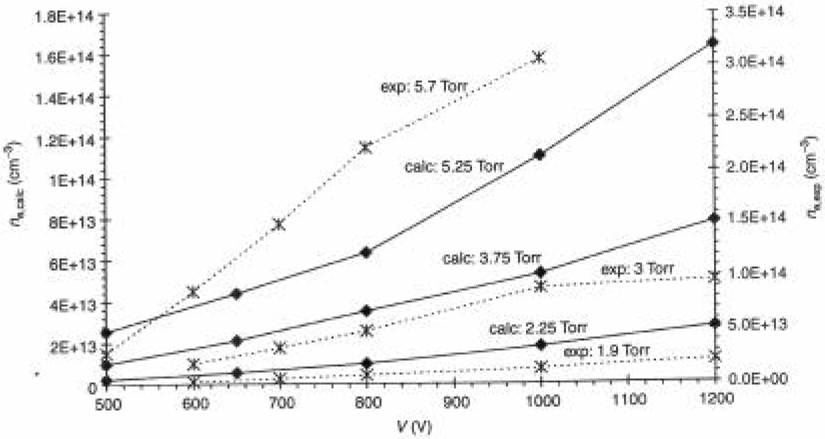

Figure 6.10 Electron number densities (at the maximum of their profiles) in a dc Grimm-type glow discharge cell, as a function of voltage at several pressures. The values calculated with our model [47] are depicted with the solid lines (left axis) whereas the Langmuir probe results [54] are represented with the dashed lines (right axis; note the different vertical scale). Reproduced from Bogaerts, A., and Gijbels, R., *Spectrochim. Acta, Part B*, 1998, **53**, 437–462, with permission of Elsevier Science

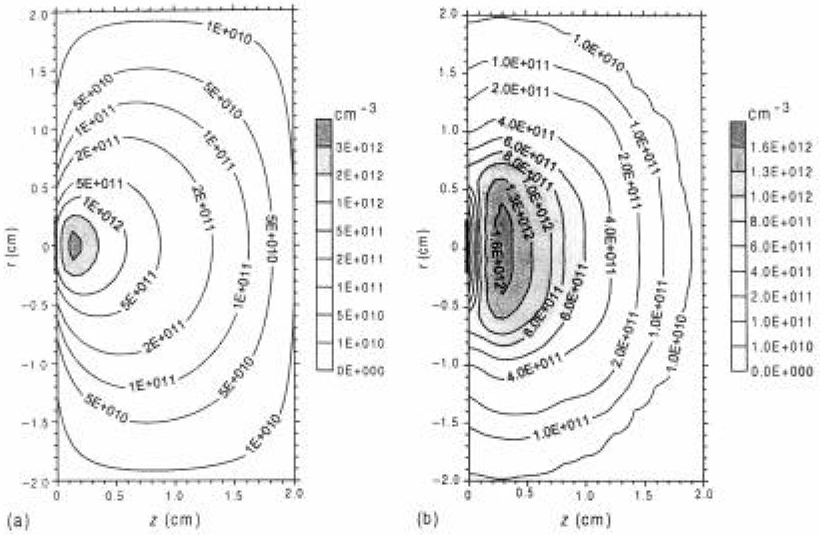

Figure 6.11 Two-dimensional density profiles of the sputtered tantalum atoms in a cylindrically symmetrical (six-way cross) glow discharge cell, at the dc conditions of 1000 V, 1 Torr and 2 mA, (a) calculated with our model and (b) measured with laser induced fluorescence (LIF). The black line at $z = 0$ indicates the cathode; the anode is formed by the other borders of the figure. Reprinted from Bogaerts, A., Wagner, E., Smith, B. W., Winefordner, J. D., Pollmann, D., Harrison, W. W., and Gijbels, R., *Spectrochim. Acta, Part B*, 1997, **52**, 205–218, with permission of Elsevier Science

a maximum at ca 1 mm from the cathode and decreases towards the cell walls. It is of the order of 10^{12} cm^{-3} under the discharge conditions under investigation, which is about four orders of magnitude lower than the argon gas atom density at 1 Torr.

The tantalum atom density has also been measured in the same cell and at the same discharge conditions as in the model, both by laser induced fluorescence (LIF) and by a combination of LIF, to obtain the relative profile, and atomic absorption spectrometry (AAS) to put an absolute number on this profile. Tantalum was used as the cathode material, because it has fluorescent lines which are in the suitable wavelength range of the laser available for the experiment [55]. The result of the LIF measurements is depicted in Figure 6.11b; the combined LIF + AAS experiments yielded values which were generally a factor of three lower [55]. The latter indicates that the experimental uncertainties can be fairly large, i.e. at least a factor of three. Comparison of Figure 6.11a and b shows that the calculated and measured tantalum atom densities are in fairly good agreement with each other. The different behavior near $z = 0$ is due to an approximation in the model, i.e. the cell used for the experiments was open at $z = 0$ (the cathode was mounted on an insertion probe), whereas the model assumed a wall at $z = 0$.

Quantitatively, the results are in very good agreement; more precisely, the calculated values lie between the LIF and the combined LIF + AAS results. Hence we can conclude that the calculated and experimental results are equal to each other within the experimental uncertainty.

The corresponding tantalum ion density, calculated for the same cell and under the same dc discharge conditions, is presented in Figure 6.12a [55]. We found that the tantalum ion and argon ion densities are characterized by the same relative profile, but the tantalum ion density is more than two orders of magnitude lower. However, as mentioned above, the ratio of tantalum atom to argon atom density was about 10^{-4}, which indicates that the tantalum atoms are more efficiently ionized in the glow discharge than the argon atoms. Indeed, in addition to electron impact ionization, the tantalum atoms can also be ionized by Penning ionization (due to argon metastable atoms) and by asymmetric charge transfer with argon ions, and the last two processes are absent for the argon atoms. Under the discharge conditions under consideration, the degree of ionization was calculated to be of the order of $10^{-5}-10^{-3}$ for argon, whereas for the sputtered atoms (tantalum, copper, etc.) typical values of about $10^{-4}-5 \times 10^{-2}$ were obtained [46,47,55].

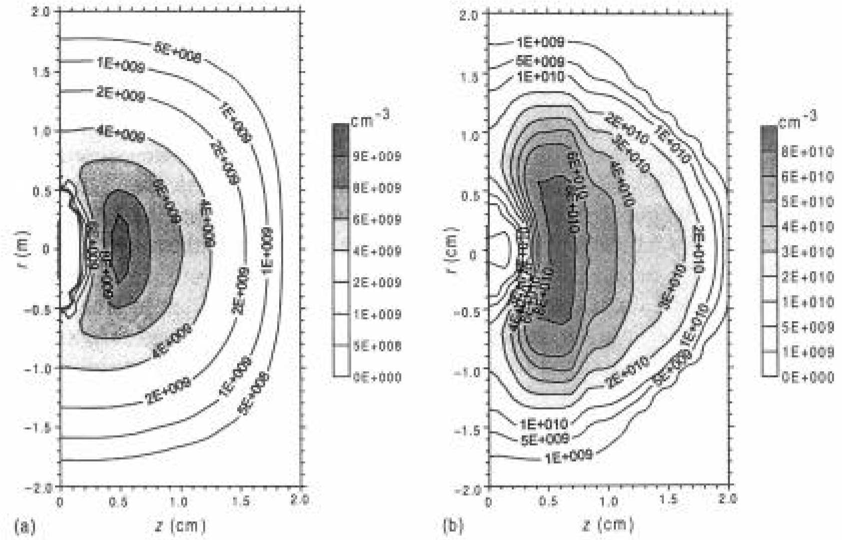

Figure 6.12 Two-dimensional density profiles of the tantalum ions in a cylindrically symmetrical (six-way cross) glow discharge cell, at the dc conditions of 1000 V, 1 Torr and 2 mA, (a) calculated with our model and (b) measured with laser induced fluorescence (LIF). Reprinted from Bogaerts, A., Wagner, E., Smith, B. W., Winefordner, J. D., Pollmann, D., Harrison, W. W., and Gijbels, R., *Spectrochim. Acta, Part B*, 1997, **52**, 205–218, with permission of Elsevier Science

To check the results of the modeling, the tantalum ion density has also been measured by LIF, and the result is shown in Figure 6.12b [55]. Calculated and experimental results qualitatively are in good agreement, but the quantitative agreement is poor. Indeed, the calculated results are a factor of almost 10 smaller than the experimental values. Since the tantalum atom densities were in fairly good agreement, this may indicate that the calculated ionization is too low, either because an important ionization mechanism is not incorporated, or because the rate coefficients for Penning ionization and asymmetric charge transfer used in the calculations are too low. The latter can indeed be the case, because these rate coefficients are very difficult to find in the literature, and the values we assumed are subject to large uncertainties. On the other hand, the experimental results are also prone to some errors, as illustrated already for the tantalum atoms (see above). Probably, the observed discrepancy is a combination of uncertainties and approximations in the model and in the experiment (e.g. conversion of LIF intensities into ion number densities). After all, the difference of a factor of 10 is maybe not so bad if one realizes that, to the authors' knowledge, such model calculations and experiments have never been carried out and confronted before.

Not only ground-state densities have been calculated with the models, also the level populations for various excited states can be obtained. Figure 6.13 illustrates the level population profiles (in one dimension) of the four lowest excited

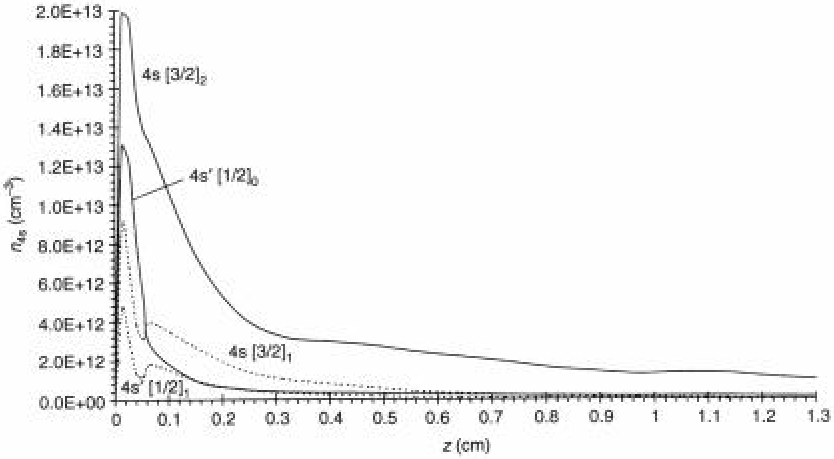

Figure 6.13 Calculated one-dimensional density profiles (at the cell axis) of the argon atoms excited to the four 4s levels, in a dc Grimm-type glow discharge cell, at 800 V, 3.75 Torr and 28 mA (solid lines, 4s metastable levels; dashed lines, 4s resonant levels). Reprinted from Bogaerts, A., and Gijbels, R., *Spectrochim. Acta, Part B*, 1998, **53**, 437–462, with permission of Elsevier Science

states of argon atoms, i.e. the 4s metastable and resonant levels, computed for the case of a Grimm-type glow discharge, under the dc conditions of 3.75 Torr, 800 V and 28 mA [47]. Only the first 1.3 cm is shown, where the densities were found to be appreciable. The two metastable levels ($4s[3/2]_2$ and $4s'[1/2]_0$; solid lines) have a slightly higher density than the two resonant levels ($4s[3/2]_1$ and $4s'[1/2]_1$; dashed lines). This is as expected, since the resonant levels can decay to the ground state by emission of radiation, whereas the metastable levels cannot decay (optically forbidden transitions). However, a large fraction of the emitted radiation from the resonant levels will again be absorbed by the ground state, leading to re-excitation. In practice, only a fraction of about $10^{-3}-10^{-4}$ of the emitted photons can really escape from the plasma under the discharge conditions under investigation [47], so that the 4s resonant levels also have a fairly high population density in comparison with other higher excited levels [47]. All 4s levels are characterized by a pronounced peak adjacent to the cathode, which is due to fast argon ion and atom impact excitation [38,47]. Indeed, the latter processes are important close to the cathode where the ions and atoms reach high energies, especially at the high voltages typical of analytical glow discharges. One-dimensional density profiles of the argon $4s[3/2]_2$ metastable levels have been measured in a Grimm-type source with AAS by Ferreira *et al.* [77]. They also found a pronounced maximum adjacent to the cathode, followed by a rapid decrease. Depending on the discharge conditions, a second maximum sometimes was observed at about 4 mm from the cathode. A similar second maximum appeared sometimes in our modeling results (e.g. [52,53]) depending on the discharge conditions and cell geometry. The value of the maximum in the experimental density profiles of Ferreira *et al.* [77] was also of the order of 10^{13} cm^{-3}, which is in excellent agreement with the results of our calculations. In Figure 6.14 the level populations for various excited copper atom and ion levels, at the maximum of their profiles, are plotted against the excitation energy of these levels, for the same dc Grimm-type conditions as in Figure 6.13 [42]. Since some of the excited levels were grouped together into effective levels (see above) with hence a much larger statistical weight, we divided the level populations by the corresponding statistical weights, to exclude this effect. It is clear that the ground-state densities of both copper atoms and ions are higher than the excited level populations, and the latter generally decrease with excitation energy. It appears that the Cu^+ $3d^9$ $4p$ $^3P_2$ level is exceptionally high compared with the other excited levels. The reason is that this level can be selectively excited by asymmetric charge transfer with argon ions, owing to good energy overlap [42]. The latter is also experimentally demonstrated, since the lines originating from this level are extremely high in comparison with other emission lines [78], which validates our calculation results.

Finally, it should be mentioned that the densities for the various plasma species calculated for an rf- and a microsecond-pulsed discharge were found to be similar to those for dc discharges [26,27,31,39,43]. The density profiles are more or

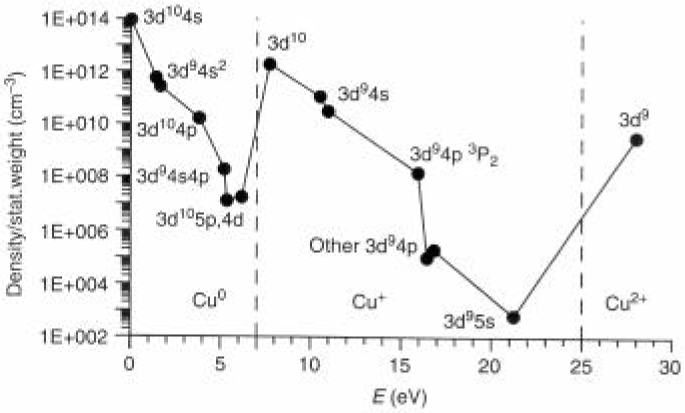

Figure 6.14 Calculated level populations at the maximum of their profiles, divided by the statistical weights of the levels, for various Cu^0 and Cu^+ levels and also for the Cu^{2+} ions, as a function of their excitation energy, in a dc Grimm-type glow discharge cell, at 800 V, 3.75 Torr and 28 mA [42]

less the same; only the absolute values can differ somewhat, depending on the discharge conditions.

6.3.4 ENERGIES OF THE PLASMA SPECIES

As mentioned before, the fluid models and collisional-radiative models are applied to the plasma species which are assumed to be in thermal equilibrium with the electric field, such as the argon atoms and copper atoms and ions in the ground state and also in excited levels, and also the slow electrons in the NG. Hence no equations are included to calculate the energy of these species, because they are assumed to have thermal energy. The plasma species which are not in hydrodynamic equilibrium, on the other hand, are described explicitly with a Monte Carlo model, and the energy distributions of these species can be computed.

Figure 6.15 presents the flux energy distribution of the electrons, at various positions from the cathode, in the VG 9000 cell at 1000 V, 0.5 Torr and 3.5 mA (dc discharge)[15,46]. The electrons leave the cathode ($z = 0$, not indicated in the figure) with low energy (assumed to be 4 eV on average [79]), but they gain energy from the electric field as they move in the CDS towards the NG. At the same time, however, they lose energy owing to collisions, so that their energy distribution spreads out from zero energy toward the maximum energy, with all energy values being more or less of equal probability. At the CDS–NG interface, being 0.24 cm away from the cathode (see Figure 6.7), this maximum energy is equal to the total discharge voltage of 1000 V. In the NG, however, the electrons

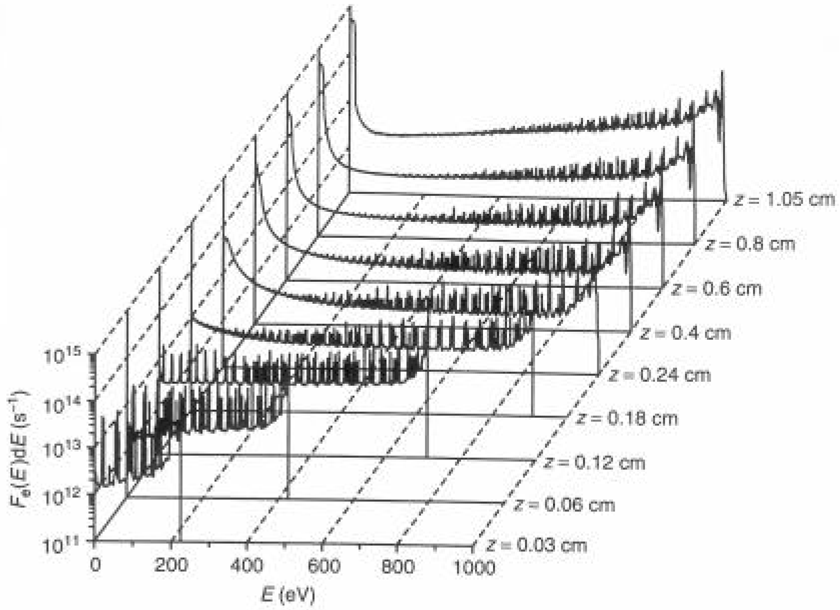

Figure 6.15 Calculated flux energy distribution of the electrons, as a function of distance from the cathode, in the VG 9000 cell, under the dc conditions of 1000 V, 0.5 Torr and 3.5 mA. Reproduced by permission of the Royal Society of Chemistry from Bogaerts, A., and Gijbels, R., *J. Anal. At. Spectrom.*, 1998, **13**, 945–953

do not gain much energy any longer from the weak electric field, but they lose their energy very efficiently owing to collisions. Hence the energy distribution shifts towards lower energies. Nevertheless, even at the end of the discharge cell, there is still a peak at maximum energy, which indicates that there are still some electrons which have traversed the entire discharge without collisions, under the discharge conditions under investigation. The present flux energy distribution of electrons is in reasonable qualitative agreement with experimental results obtained with a retarding field analyzer in the NG of a helium glow discharge at pressures of 10–15 Torr and a few hundred volts discharge voltage [80]. Indeed, it was found that most electrons have low energies, but a small peak is observed at maximum energy. This shows that our calculation results can be considered to be realistic.

In contrast to the electron flux energy distribution, the energy distribution of the argon ions is not characterized by a peak at maximum energy. This appears from Figure 6.16a, where the calculated flux energy distribution of the argon ions is depicted for several distances from the cathode in the CDS, under the same discharge conditions as in Figure 6.15 [15,46]. The argon ions are assumed

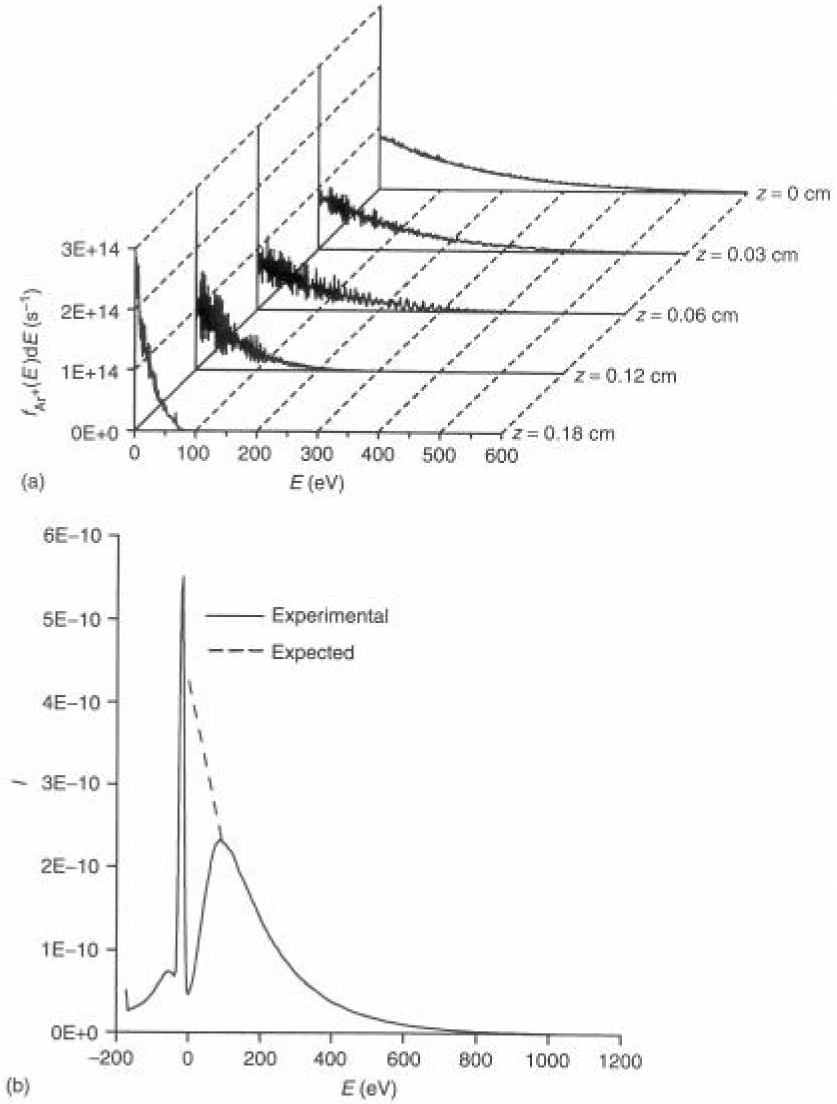

Figure 6.16 Flux energy distributions of the argon ions in a dc discharge, in the VG 9000 cell: (a) calculated in the CDS, as a function of distance from the cathode, for 1000 V, 0.5 Torr and 3.5 mA; (b) measured at the cathode, at 1000 V and 3 mA (pressure unknown). Reproduced by permission of the Royal Society of Chemistry from Bogaerts, A., and Gijbels, R., *J. Anal. At. Spectrom.*, 1998, **13**, 945–953

to have thermal energies in the NG, but when they enter the CDS they gain energy from the electric field. However, they also lose energy owing to collisions. It appears that the collisions of the ions, which mainly are elastic scattering and symmetric charge transfer collisions, are more frequent and more efficient for losing energy than the collisions of the electrons (mainly ionization and excitation), because most argon ions have fairly low energies when they arrive at the cathode ($z = 0$ cm).

The energy distribution of the argon ions bombarding the cathode has been measured in a similar cell, in reversed geometry so that the ions are sampled through a hole in the cathode, and under similar discharge conditions to those used for the calculations [58]. These measurements were performed with the VG 9000 double focusing glow discharge mass spectrometer, by keeping the magnetic field constant and varying the acceleration voltage. The results are shown in Figure 6.16b [15,46]. A dip was obtained at low energy and a peak at negative energy, which were probably the results of experimental artifacts; it was suggested that low-energy ions were subject to charge transfer collisions (for which the cross-section is, indeed, larger at low energies) immediately outside the discharge cell, in the acceleration region of the mass spectrometer. This gives rise to some loss for low-energy ions, explaining the dip, because the ions disappear from the energy distribution, as well as some production (i.e. a peak) at negative energy, because these ions have not attained the maximum acceleration voltage. Therefore, the expected 'real' energy distribution is indicated by the dashed line in Figure 6.16b, which agrees qualitatively with the calculated results.

As mentioned earlier in this chapter, the collision processes of the argon ions with thermal argon atoms in the CDS can give rise to the production of 'fast' (i.e. nonthermal) argon atoms, due to exchange of energy. These fast argon atoms can continue in the same direction as the ions, towards the cathode, or they can be scattered in another direction, but at least a fraction of them will be able to arrive at the cathode before again being thermalized owing to collisions. Because these fast argon atoms can, themselves, also create new fast argon atoms due to energy exchange in elastic collisions, the flux of fast argon atoms traveling through the CDS is fairly high. This can be seen in Figure 6.17, where the calculated flux energy distributions of the fast argon atoms in the CDS, at various positions from the cathode, are presented [15,46]. The flux is, indeed, more than an order of magnitude higher than the argon ion flux. The energy distribution qualitatively looks very similar to the argon ion energy distribution, but it is shifted towards lower energies (note that the energy scale is cut at 100 eV), because the argon atoms cannot gain energy from the electric field; they can only lose their energy in collisions.

In addition to the argon ions and fast argon atoms, also the ions of the cathode material travel through the CDS and can bombard the cathode. Figure 6.18a shows the calculated energy distribution of the cathode copper ion flux in the CDS, at various positions from the cathode, for the same discharge conditions

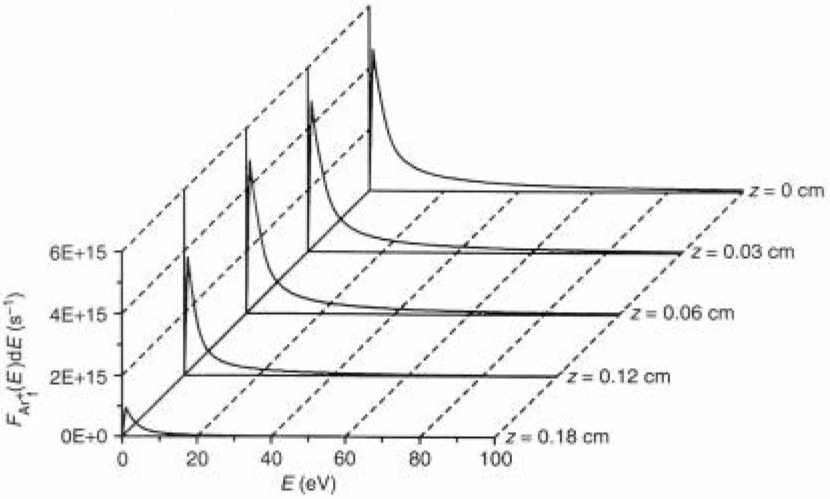

Figure 6.17 Calculated flux energy distribution of the fast argon atoms in the CDS, as a function of distance from the cathode, in the VG 9000 cell, at the dc conditions of 1000 V, 0.5 Torr and 3.5 mA. Reproduced by permission of the Royal Society of Chemistry from Bogaerts, A., and Gijbels, R., *J. Anal. At. Spectrom.*, 1998, **13**, 945–953

as in Figure 6.16 [15,46]. The copper ions also have thermal energy in the NG, where most of them were formed, but when they diffuse into the CDS they gain energy from the electric field and are accelerated towards the cathode. In contrast to the argon ions, they do not lose their energy very efficiently in collisions. Therefore, they are characterized by a pronounced peak at maximum energy.

This pronounced peak is also experimentally observed (Figure 6.18b) [58]. These experiments were performed with the same technique as explained above. Since the pressure could actually not be measured inside the glow discharge cell of this mass spectrometer, three estimated pressure values are indicated for the three experimental energy distributions. Exact quantitative comparison therefore cannot be carried out, but qualitative agreement between calculated and experimental results, at least, is reached.

6.3.5 INFORMATION ABOUT COLLISION PROCESSES IN THE PLASMA

Since the Monte Carlo models describe the behavior of the plasma species explicitly, they can give information about the individual collision processes in the plasma. The various collision rates of the plasma species (i.e. ionization, excitation, elastic collisions, charge transfer, etc.) have been calculated as a function of the position in the discharge; the results (in one and in two dimensions) have been

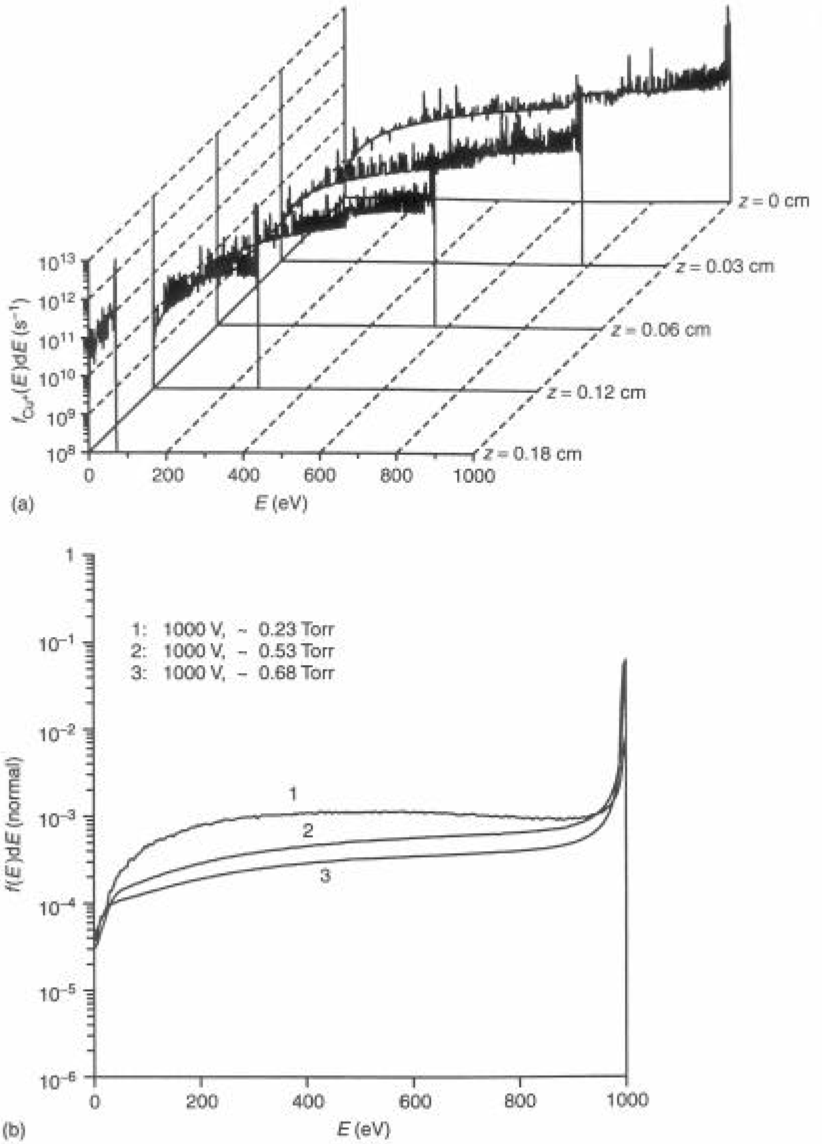

Figure 6.18 Flux energy distributions of the copper ions in a dc discharge, in the VG 9000 cell: (a) calculated in the CDS, as a function of distance from the cathode, for 1000 V, 0.5 Torr and 3.5 mA; (b) measured at the cathode, at 1000 V and three pressure values. Reproduced by permission of the Royal Society of Chemistry from Bogaerts, A., and Gijbels, R., *J. Anal. At. Spectrom.*, 1998, **13**, 945–953

presented many times in our previous papers (e.g. [23–27,31,33,38,39,42–47,52]), and will therefore not be repeated here. Instead, some data will be given concerning the relative importance of these processes. Moreover, ionization will be discussed in somewhat more detail, since it is considered to be the most important process in the glow discharge.

Ionization of the argon gas atoms is the process which makes the glow discharge self-sustaining. The ionization occurs mainly by electron impact; at high discharge voltages (ca 1000 V), however, fast argon ion and atom impact ionization play a non-negligible role [33]. Figure 6.19 presents the ionization rates according to these three mechanisms, in the VG 9000 cell under the same dc conditions as in Figure 6.7 [25]. Electron impact ionization is especially important in the NG, whereas fast argon ion and atom impact ionization occur only adjacent to the cathode. Integrated over the entire discharge region, the relative contributions of electron, ion and atom impact ionization were calculated to be typically about 90, 2 and 8%, respectively. Hence electron impact ionization is still clearly dominant, because it can take place throughout the entire discharge, whereas ion and atom impact ionization occur only close to the cathode, where these species can reach high energies. Nevertheless, it was found really necessary to incorporate the latter processes in our models, in order to be able to reproduce the correct current–pressure–voltage relations at high voltages (see the

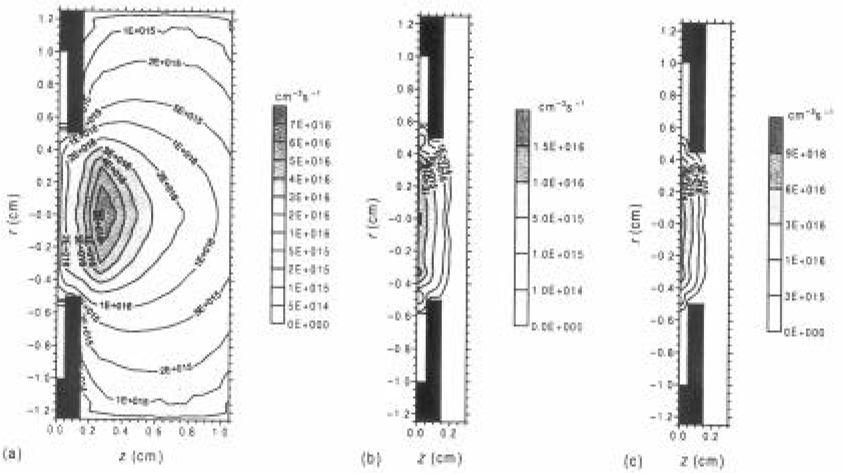

Figure 6.19 Calculated ionization rates of the argon atoms in the VG 9000 cell, under the dc conditions of 1000 V, 0.5 Torr and 3.5 mA: (a) by electron impact ionization in the entire discharge; (b) by fast argon ion impact ionization in the CDS; (c) by fast argon atom impact ionization in the CDS. Reprinted with permission from Bogaerts, A., Gijbels, R., and Goedheer, W. J., *Anal. Chem.*, 1996, **68**, 2296–2303, Copyright 1996 American Chemical Society

discussion concerning Figure 6.3). On the other hand, stepwise electron impact ionization from the metastable levels and metastable atom–metastable atom collisions leading to the ionization of one of the atoms were found to be generally negligible under the discharge conditions under investigation. Their contribution is estimated to be lower than 1%.

As far as the sputtered atoms are concerned, electron impact ionization also takes place, but it is of minor importance compared with Penning ionization and asymmetric charge transfer, as explained above. The ionization rates due to these three mechanisms are presented in Figure 6.20 [45], for the same conditions and cell geometry as in Figure 6.19. Integrated over the total discharge region, the three ionization processes contribute typically about 2–4% (electron impact), 40–85% (Penning ionization) and 10–60% (asymmetric charge transfer). These values depend fairly strongly on the cell geometry, the kind of sputtered material (i.e. for some elements whose ions have no energy levels overlapping with the argon gas ions, asymmetric charge transfer is absent) and the discharge conditions. Penning ionization is clearly dominant at low pressures, whereas asymmetric charge transfer gains importance at higher pressures.

The model predicts also the relative contributions of the different populating and depopulating processes for the argon atom and copper atom and ion excited levels, such as electron, ion and atom impact excitation, de-excitation and ionization for all levels, electron–ion radiative and three-body recombination, radiative decay, etc. [38,39,42,43].

For the argon excited levels [38,39], radiative decay was calculated to be dominant, both as production and loss process for the low-lying levels, although

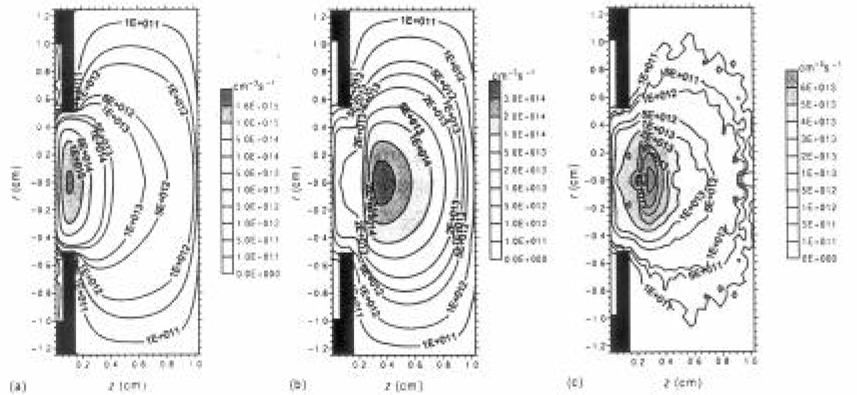

Figure 6.20 Calculated ionization rates of the sputtered copper atoms in the VG 9000 cell, under the dc conditions of 1000 V, 0.5 Torr and 3.5 mA: (a) by Penning ionization; (b) by asymmetric charge transfer; (c) by electron impact ionization. Reproduced with permission from Bogaerts, A., and Gijbels, R., *Anal. Chem.*, 1996, **68**, 2676–2685, Copyright 1996 American Chemical Society

electron, fast argon ion and fast argon atom impact excitation from the ground state were also found to be important production processes. The 4s metastable levels, which cannot decay to the ground state by emission of radiation, are mainly destroyed by metastable atom–metastable atom collisions, by Penning ionization of sputtered atoms, by electron impact excitation to the nearby 4s resonant levels and also by diffusion and subsequent de-excitation at the cell walls [38]. The highly excited levels, on the other hand, appear to be primarily populated and depopulated by electron, argon ion and atom impact excitation and de-excitation from and towards nearby levels.

In the case of the copper atoms [42,43], it was found that sputtering from the cathode is the dominant production process for the copper ground-state atoms, whereas depopulation is mainly caused by ionization (especially Penning ionization and asymmetric charge transfer) and by excitation to copper atom excited levels. The copper atom excited levels are mainly formed by electron impact excitation from the copper atom ground state and by radiative decay from higher excited levels. The major loss process for the copper atom excited levels is found to be radiative decay to lower levels. The copper ions, both in the ground state and in the $3d^9$ 4s metastable levels, are predominantly formed by Penning ionization. Loss of the copper ion ground state occurs by electron impact excitation to higher levels, and also by electron impact ionization to Cu^{2+} and by electron–ion three-body recombination. The copper ion metastable levels are mainly depopulated by electron impact de-excitation to the ground state. The Cu^+ $3d^9$ 4p $^3P_2$ level appears to be almost exclusively created by asymmetric charge transfer, whereas the other $3d^9$ 4p levels are formed by electron impact excitation from the Cu^+ $3d^9$ 4s metastable levels and the copper ion ground state. The highly excited copper ion levels were found to be primarily depopulated by radiative decay to the lower levels. More information about the relative importance of the various populating and depopulating processes of argon and copper excited levels can be found in the literature [38,39,42,43].

The results presented above for the dc mode are in general, at least qualitatively, similar for the rf and pulsed operation modes, except that the collision processes will vary as a function of time.

6.3.6 INFORMATION ABOUT SPUTTERING AT THE CATHODE

In addition to making predictions about collision processes in the plasma, the models can also give more information about the sputtering process at the cathode. Indeed, the energy distributions of the species bombarding the cathode, namely argon and cathode ions and fast argon atoms, (see Figures 6.16, 6.17 and 6.18) are calculated over the entire cathode surface. When combining these flux energy distributions with an equation for the sputtering yield as a function of bombarding energy and type of bombarding particle, the flux of sputtered atoms, as a function of radial position, can be calculated. From this, the crater profile at the cathode, after a certain time of sputtering, can be obtained [46,59].

A typical calculated crater profile, calculated for the VG 9000 cell at 1000 V, 0.5 Torr and 3.5 mA (dc conditions), is shown in Figure 6.21a. For good depth-profiling analysis, it is logical that flat crater profiles are desirable; if not, sample atoms originating from different depths enter the plasma simultaneously and the depth resolution of the analysis is worsened. The crater profile presented in Figure 6.21a is therefore not ideal for depth profiling. Indeed, it is much deeper at the edges than in the center (so-called 'crater edge effect'), the crater walls are not steep and the crater bottom is not flat. Moreover, there is a small rim outside the crater profile. This calculated result is, however, often encountered in glow discharge depth profiling with the VG 9000 cell, which is actually not designed for concentration depth profiling, but for sensitive trace analysis of homogeneous samples. Figure 6.21b illustrates a typical measured crater profile, obtained in the VG 9000 cell, under similar discharge conditions as in Figure 6.21a [60]. The crater profile also displays the crater edge effect, the crater walls are not very steep, although not so pronounced as in the calculated result, and there

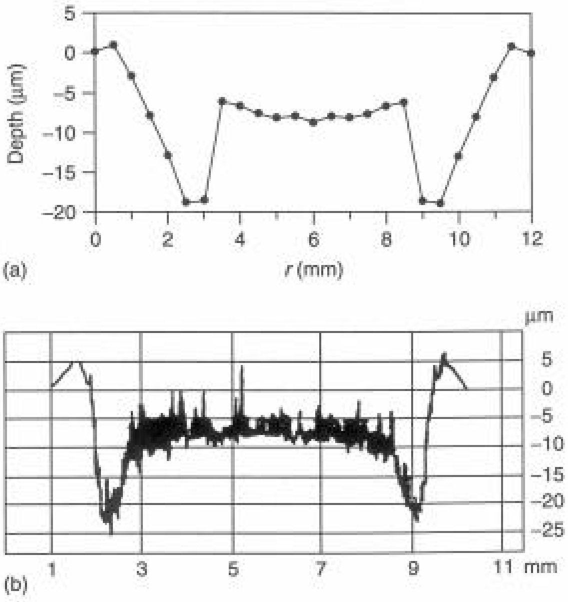

Figure 6.21 Crater profiles after 45 min of sputtering on a copper cathode, in a dc discharge, in the VG 9000 cell, (a) calculated at 1000 V, 0.5 Torr and 3.5 mA and (b) measured at 1000 V and 3 mA (pressure unknown). Reproduced by permission of the Royal Society of Chemistry from Bogaerts, A., and Gijbels, R., *J. Anal. At. Spectrom.*, 1998, **13**, 945–953

is also a rim outside the crater profile. Hence the calculated and experimental crater profiles are in reasonable qualitative agreement. Moreover, the absolute values on the y-axis show that the results are also in satisfactory quantitative agreement. This example demonstrates that the model is able to make predictions about crater profiles to be expected for a specific cell geometry and certain discharge conditions. By applying some modifications to this geometry and/or to the discharge conditions, the crater profile could be optimized. In practice, this optimization procedure is commonly performed by trial and error. This can be expensive and time consuming, and often leads to disappointing results. However, the optimization can now in principle also be simulated with the model, prior to building the new cell, which is much cheaper and more efficient.

From the energy distributions of the argon ions, fast argon atoms and copper ions bombarding the cathode, the relative contributions of these species to the sputtering process can be calculated. From the large flux of fast argon atoms, it can be expected that they have a dominant role in sputtering, in spite of the lower bombarding energies. Indeed, their contribution to the sputtering amounts to about 40–70% (increasing with decreasing pressure and voltage). The argon ions generally contribute about 20–40%. The role of the copper ions (called 'self-sputtering') is of minor importance at low voltages and pressures, but they can have a contribution of as much as 50% at the highest voltages and pressures investigated (i.e. 5 Torr, 1200 V, ca 100 mA) [47]. Indeed, as was shown in Figure 6.18a and b, the copper ion energy distribution has a distinct peak at maximum energy, and since the sputtering efficiency increases with rising energy of the bombarding species, it can indeed be expected that the copper ions have a non-negligible contribution in spite of their lower flux. This was also suggested earlier, based on experimental results [58].

The above crater profiles are shown for the VG 9000 cell, because we had experimental data available, but it should be mentioned that glow discharge depth profiling is more often performed with the Grimm-type cell, under GD-OES conditions (at higher pressure and current), where much higher erosion rates are obtained. We calculated erosion rates for typical GD-OES discharge conditions [47], and found that the absolute values are in reasonable agreement with experimental data found in the GD-OES literature [61,62]. Hence this suggests that our models present a realistic picture of the sputtering in a glow discharge.

Our calculations for the rf mode indicated that there is slightly more sputtering than in the dc mode for the same conditions of power and pressure [43]. The latter was in excellent agreement with experiment data [49]. In the microsecond-pulsed mode, the calculated net amount of erosion during one pulse was also found to be in good correspondence with the experimental values. Moreover, we found that the fast argon atoms play the most important role for sputtering in the first 1–3 μs of the pulse, whereas the copper ions appear to become dominant after 3 μs (so-called self-sputtering).

6.3.7 OPTICAL EMISSION INTENSITIES

From the collisional-radiative models which describe the behavior of various excited levels of argon atoms, copper atoms and copper ions [38,39,42,43] we were able to calculate optical emission intensities in the glow discharge (i.e. the product of the level populations and the Einstein transition probabilities for radiative decay) [64–66].

Figure 6.22a presents the calculated argon atomic optical emission spectrum for a Grimm-type glow discharge, integrated over the discharge axis, to simulate end-on observation. It is clear that the lines in the region of 700–1000 nm (i.e. the so-called red lines, corresponding to 4p → 4s transitions) dominate in the spectrum. Figure 6.22b depicts the argon atomic spectrum, found in the literature [67] and measured in a hollow cathode glow discharge at a current of 150 mA and a pressure of 1 Torr. In spite of the completely different discharge conditions, both spectra have a similar appearance. Indeed, the intensities of the various lines are comparable. This is not straightforward, in view of the large number of populating and depopulating processes taking place for the various levels, and the uncertainties in the cross-sections and transition probabilities used in the model. In the near future, we plan to perform a detailed comparison between calculated and measured optical emission spectra under exactly the same conditions, both for the dc mode and the rf mode (in the framework of an EC Thematic Network on Glow Discharge Spectrometry).

In order to study the relative importance of various excitation mechanisms, we have also compared our calculated spectral line intensities, as a function of distance from the cathode, with measurements at exactly the same discharge conditions and cell geometry [66]. Figure 6.23a shows the calculated spatial distributions of some selected Ar I, Ar II and Cu I lines, at 0.6 Torr and five different currents and voltages, and the corresponding experimental results [81] are plotted in Figure 6.23b. It appears that very good agreement has been reached, which suggests that our model takes into account the correct excitation mechanisms and uses realistic cross-sections, and that it can therefore give more or less reliable predictions for GD-OES.

6.3.8 PREDICTION OF THE EFFECT OF THE CELL GEOMETRY

The models can be applied to various kinds of cell geometries, such as shown above for the VG 9000 flat cell, a Grimm-type cell, a six-way cross glow discharge cell or other types of cell geometries, as long as the cell is cylindrically symmetrical. For example, Figure 6.24a and b show the calculated copper atom density distribution for an arbitrary cell, with a flat and a pin-type of cathode [57]. In the cell with a flat cathode, the plasma is most intense in front of the cathode, whereas in a cell with a pin cathode, the plasma forms a kind of ring around

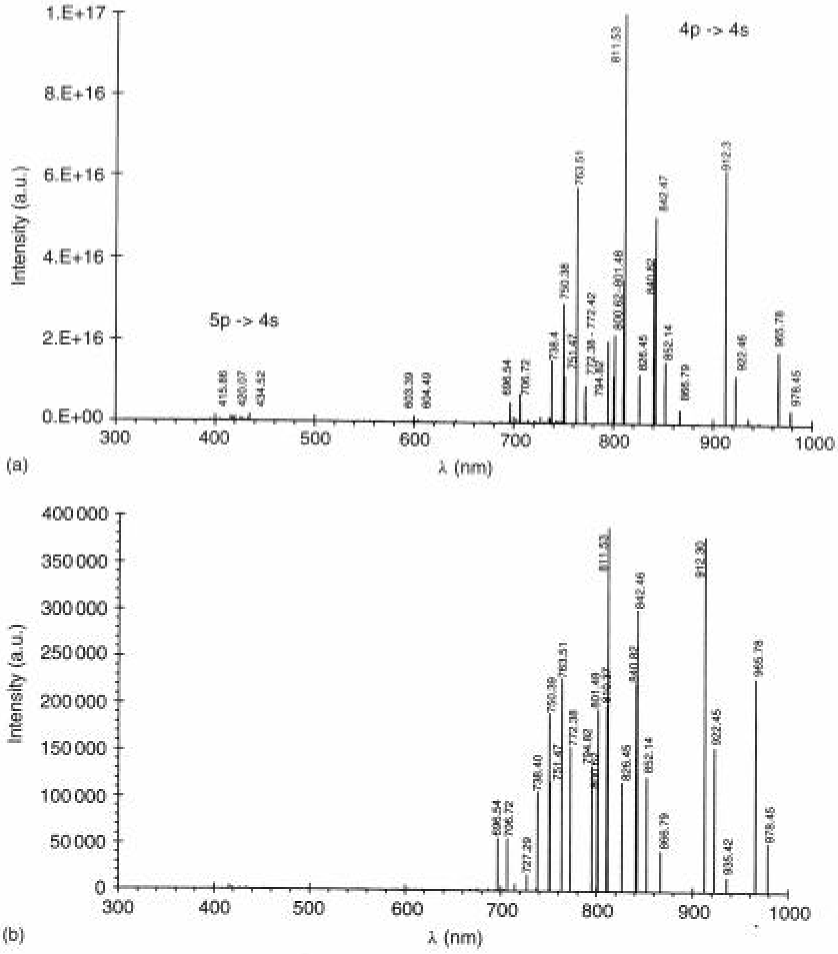

Figure 6.22 Optical emission spectra of the argon atoms, in a dc discharge: (a) calculated in a Grimm-type glow discharge cell, integrated over the entire cell axis to simulate end-on observation, at 800 V, 3.75 Torr and 28 mA; (b) measured in a hollow cathode glow discharge at 150 mA and 1 Torr. Reprinted from Bogaerts, A., Gijbels, R., and Vlcek, J., *Spectrochim. Acta, Part B*, 1998, **53**, 1517–1526, with permission of Elsevier Science

the pin. In that work [57], the ion fluxes bombarding the exit slit to the mass spectrometer were calculated for the above two cell designs, which gives an idea about the ion intensities in the mass spectrum. This illustrates that the models can in principle be applied to predict the effect of cell geometry, as a help for the design of new cells.

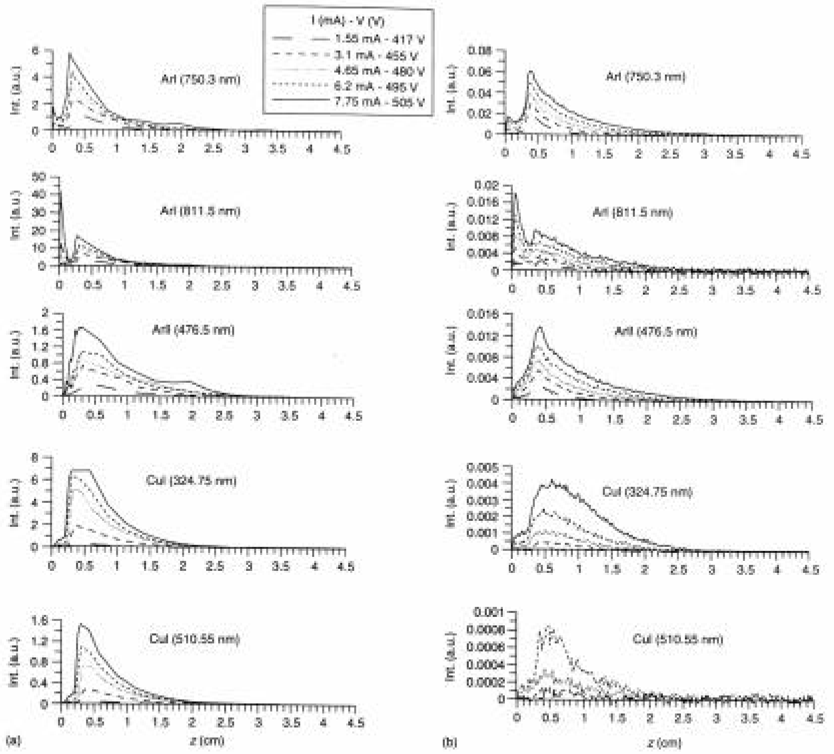

Figure 6.23 Optical emission intensities as a function of distance from the cathode, in a dc cylindrically symmetrical glow discharge cell, at a pressure of 0.6 Torr and five different currents and voltages, for the lines Ar I (750.3 nm), Ar I (811.5 nm), Ar II (476.5 nm), Cu I (324.75 nm) and Cu I (510.55 nm). (a) Calculated and (b) measured values [66]

6.3.9 PREDICTION OF RELATIVE SENSITIVITY FACTORS IN GDMS

Finally, as a spin-off, we have used our models to explain experimentally observed differences in relative sensitivity factors (RSFs) in GDMS [69]. Since the cross-sections of asymmetric charge transfer ionization of different elements are not available in the literature, a model was developed for calculating RSFs based on transport and Penning ionization only, since electron impact ionization is of minor importance (see above), to test the influence of asymmetric charge transfer. A systematic investigation for 42 elements showed that a correlation exists between the discrepancy between calculated and experimental RSFs on the one hand, and the availability of suitable energy levels for asymmetric charge transfer on the other.

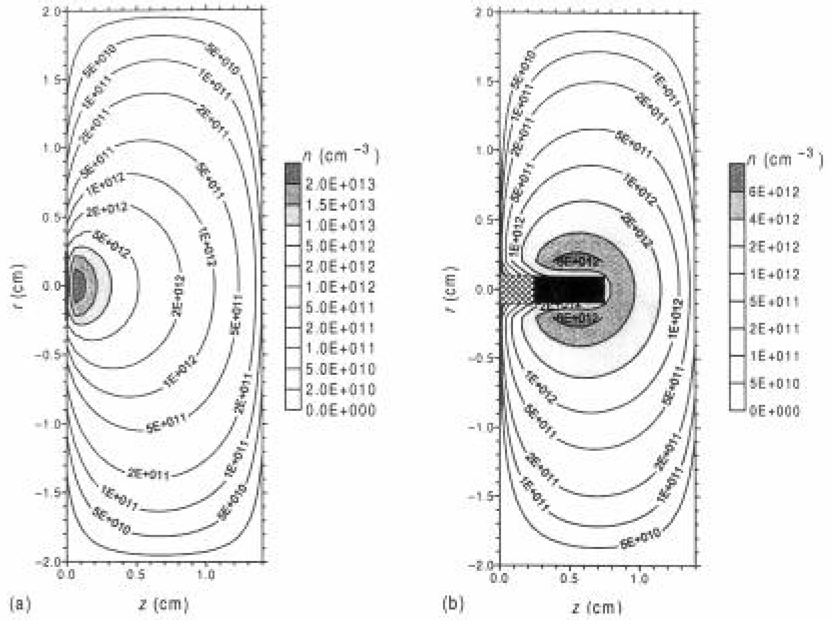

Figure 6.24 Calculated two-dimensional density profiles of the sputtered copper atoms, in a dc discharge (a) with flat cathode (at 1000 V, 2.2 mA and 1 Torr) and (b) with pin-type of cathode (at 1000 V, 2.2 mA and 0.7 Torr). Reprinted from Bogaerts, A., and Gijbels, R., *J. Am. Soc. Mass Spectrom.*, 1997, **8**, 1021–1029, with permission of Elsevier Science

This strongly suggests that, in addition to transport and Penning ionization, especially the occurrence or nonoccurrence of asymmetric charge transfer can explain the differences in RSFs among different elements. More information about this investigation can be found elsewhere [69].

6.4 CONCLUSION

It has been illustrated with some typical examples what can be calculated with the models described for the case of several types of glow discharges. In general, it can be concluded that the models present a realistic picture of the glow discharge and can predict qualitative trends. Exact quantitative predictions, however, cannot yet be expected, because there are too many uncertainties in the input data, such as the cross-sections. Therefore, exact computer prediction of an analytical measurement is not yet realistic, but the models can certainly give a better insight into what is important in the plasma, which might also help to improve the analytical performance of glow discharges.

6.5 REFERENCES

[1] Berezhnoi, S. V.; Kaganovich, I. D.; Tsendin, L. D.; Schweigert, V. A. *Appl. Phys. Lett.*, 1996, **69**, 2341–2343.

[2] Lee, Y. T.; Lieberman, M. A.; Lichtenberg, A. J.; Bose, F.; Baltes, H.; Patrick, R. *J. Vac. Sci. Technol. A*, 1997, **15**, 113–126.

[3] Boeuf, J.-P. *J. Appl. Phys.*, 1988, **63**, 1342–1349.

[4] Passchier, J. D. P.; Goedheer, W. J. *J. Appl. Phys.*, 1993, **73**, 1073–1079.

[5] Yachi, S.; Kitamura, Y.; Kitamori, K.; Tagashira, H. *J. Phys. D*, 1988, **21**, 914–921.

[6] Loffhagen, D.; Winkler, R. *J. Comput. Phys.*, 1994, **112**, 91–101.

[7] Kushner, M. J. *IEEE Trans. Plasma Sci.*, 1986, **14**, 188–196.

[8] Donko, Z.; Rozsa, K.; Tobin, R. C. *J. Phys. D*, 1996, **29**, 105–114.

[9] Surendra, M.; Graves, D. B. *IEEE Trans. Plasma Sci.*, 1991, **19**, 144–157.

10] Smith, H. B.; Charles, C.; Boswell, R. W.; Kuwahara, H. *J. Appl. Phys.*, 1997, **82**, 561–565.

11] Yan, M.; Goedheer, W. J. *IEEE Trans. Plasma Sci.*, 1999, **27**, 1399–1405.

12] Surendra, M.; Graves, D. B.; Jellum, G. M. *Phys. Rev. A* 1990, **41**, 1112–1125.

13] Huang, F. Y.; Kushner, M. J. *J. Appl. Phys.*, 1995, **78**, 5909–5918.

14] Donko, Z. *Phys. Rev. E*, 1998, **57**, 7126–7137.

15] Bogaerts, A.; Gijbels, R. *J. Anal. At. Spectrom.*, 1998, **13**, 945–953.

16] Bogaerts, A.; Gijbels, R. *J. Anal. At. Spectrom.*, 2000, **15**, 1191–1201.

17] Vieth, W.; Huneke, J. C. *Spectrochim. Acta, Part B*, 1991, **46**, 137–153.

18] Valles-Abarca, J. A.; Gras-Marti, A. *J. Appl. Phys.*, 1984, **55**, 1370–1378.

19] Mason, R. S.; Pichilingi, M. *J. Phys. D.*, 1994, **27**, 2363–2371.

20] Fiala, A.; Pitchford, L. C.; Boeuf, J. P.; Baude, S. *Spectrochim. Acta, Part B*, 1997, **52**, 531–536.

21] Ganeev, A. A.; Vergizova, V. S.; Voronov, M. V.; Slyadnev, M. N.; Sholupov, S. E.; Stroganov, A. A., Glow discharge pulse ionization of residue in thin-walled metallic hollow cathode with time-of-flight spectrometry. Experimental and modeling investigation, Poster at 2000 Winter Conference on Plasma Spectrochemistry, Fort Lauderdale, FL, January 2000.

22] Bogaerts, A.; Gijbels, R. *Anal. Chem.*, 1997, **69**, 719A–727A.

23] Bogaerts, A.; van Straaten, M.; Gijbels, R. *Spectrochim. Acta, Part B*, 1995, **50**, 179–196.

24] Bogaerts, A.; Gijbels, R.; Goedheer, W. J. *J. Appl. Phys.*, 1995, **78**, 2233–2241.

25] Bogaerts, A.; Gijbels, R.; Goedheer, W. J. *Anal. Chem.*, 1996, **68**, 2296–2303.

26] Bogaerts, A.; Gijbels, R.; Goedheer, W. J. *Jpn. J. Appl. Phys.*, 1999, **38**, 4404–4415.

27] Bogaerts, A.; Gijbels, R. *J. Anal. At. Spectrom.*, 2000, **15**, 895–905.

28] Jogwich, M.; Huber, B. A.; Wiesemann, K. *Z. Phys. D*, 1990, **17**, 171–179.

29] Gummel, H. K. *IEEE Trans. Plasma Sci.*, 1964, **11**, 455–465.

30] Scharfetter, D. L.; Gummel, H. K. *IEEE Trans. Electron. Devices*, 1969, **16**, 64–77.

31] Bogaerts, A.; Yan, M.; Gijbels, R.; Goedheer, W. *J. Appl. Phys.*, 1999, **86**, 2990–3001.

32] Bogaerts, A.; Gijbels, R. *J. Appl. Phys.*, 1999, **86**, 4124–4133.

33] Bogaerts, A.; Gijbels, R. *J. Appl. Phys.*, 1995, **78**, 6427–6431.

34] Bogaerts, A.; Gijbels, R. *IEEE Trans. Plasma Sci.*, 1999, **27**, 1406–1415.

35] Bogaerts, A.; Gijbels, R.; Serikov, V. V. *J. Appl. Phys.*, 2000, **87**, 8334–8344.

36] Holstein, T. *Phys. Rev.*, 1951, **83**, 1159–1168.

37] Walsh, P. J. *Phys. Rev.*, 1959, **116**, 511–515.

38] Bogaerts, A.; Gijbels, R.; Vlcek, J. *J. Appl. Phys.*, 1998, **84**, 121–136.

39] Bogaerts, A.; Gijbels, R. *Spectrochim. Acta, Part B*, 2000, **55**, 263–278.

40] Matsunami, N.; Yamamura, Y.; Itikawa, Y.; Itoh, N.; Kazumata, Y.; Miyagawa, S.; Morita, K.; Shimizu, R.; Tawara, H. *At. Data Nucl. Data Tables*, 1984, **31**, 1–80.

[41] Bogaerts, A.; van Straaten, M.; Gijbels, R. *J. Appl. Phys.*, 1995, **77**, 1868–1874.

[42] Bogaerts, A.; Gijbels, R.; Carman, R. J. *Spectrochim. Acta, Part B*, 1998, **53**, 1679–1703.

[43] Bogaerts, A.; Gijbels, R. *Spectrochim. Acta, Part B*, 2000, **55**, 279–297.

[44] Bogaerts, A.; Gijbels, R. *J. Appl. Phys.*, 1996, **79**, 1279–1286.

[45] Bogaerts, A.; Gijbels, R. *Anal. Chem.*, 1996, **68**, 2676–2685.

[46] Bogaerts, A. *PhD Dissertation*, University of Antwerp, 1996.

[47] Bogaerts, A.; Gijbels, R. *Spectrochim. Acta, Part B*, 1998, **53**, 437–462.

[48] Bogaerts, A.; Gijbels, R.; Goedheer, W. *Spectrochim. Acta, Part B*, 1999, **54**, 1335–1350.

[49] Bogaerts, A.; Wilken, L.; Hoffmann, V.; Gijbels, R.; Wetzig, K. *Spectrochimica Acta Part B*, 2002, **57**, 109–119.

[50] Yang, C.; Harrison, W. W. Personal communication.

[51] Aston, F. W. *Proc. R. Soc. London, Ser. A*, 1907, **79**, 80.

[52] Bogaerts, A.; Gijbels, R. *Phys. Rev. A*, 1995, **52**, 3743–3751.

[53] Bogaerts, A.; Guenard, R. D.; Smith, B. W.; Winefordner, J. D.; Harrison, W. W.; Gijbels, R. *Spectrochim. Acta, Part B*, 1997, **52**, 219–229.

[54] Bogaerts, A.; Quentmeier, A.; Jakubowski, N.; Gijbels, R. *Spectrochim. Acta, Part B*, 1995, **50**, 1337–1349.

[55] Bogaerts, A.; Wagner, E.; Smith, B. W.; Winefordner, J. D.; Pollmann, D.; Harrison, W. W.; Gijbels, R. *Spectrochim. Acta, Part B*, 1997, **52**, 205–218.

[56] Bogaerts, A.; Gijbels, R. *J. Anal. At. Spectrom.*, 1997, **12**, 751–759.

[57] Bogaerts, A.; Gijbels, R. *J. Am. Soc. Mass Spectrom.*, 1997, **8**, 1021–1029.

[58] van Straaten, M.; Bogaerts, A.; Gijbels, R. *Spectrochim. Acta, Part B*, 1995, **50**, 583–605.

[59] Bogaerts, A.; Gijbels, R. *Spectrochim. Acta, Part B*, 1997, **52**, 765–778.

[60] Jonkers, C. *PhD Dissertation*, University of Antwerp, 1995.

[61] Bogaerts, A.; Wilken, L.; Hoffmann, V.; Gijbels, R.; Wetzig, K. *Spectrochim. Acta Part B*, 2001, **56**, 551–564.

[62] Hocquaux, H. Thin film analysis, in Marcus, R. K. (Ed.), *Glow Discharge Spectroscopies*, Plenum, New York, 1993, p. 346.

[63] Bogaerts, A.; Gijbels, R. *J. Anal. At. Spectrom.*, 2001, **16**, 239–249.

[64] Bogaerts, A.; Gijbels, R.; Vlcek, J. *Spectrochim. Acta, Part B*, 1998, **53**, 1517–1526.

[65] Bogaerts, A.; Gijbels, R. *J. Anal. At. Spectrom.*, 1998, **13**, 721–726.

[66] Bogaerts, A.; Donko, Z.; Kutasi, K.; Bano, G.; Pinhao, N.; Pinheiro, M. *Spectrochim. Acta, Part B*, 2000, **55**, 1465–1479.

[67] Gray, D. E. *American Institute of Physics Handbook*, 3rd Edition, McGraw-Hill, New York, 1972.

[68] Rozsa, K.; Gallagher, A.; Donko, Z. *Phys. Rev. E*, 1995, **52**, 913–918.

[69] Bogaerts, A.; Gijbels, R. *J. Anal. At. Spectrom.*, 1996, **11**, 841–847.

[70] Peterson, L. R.; Allen, J. E., Jr. *J Chem. Phys.*, 1972, **56**, 6068–6076.

[71] Phelps, A. V. *J. Phys. Chem. Ref. Data*, 1991, **20**, 557–573.

[72] van Straaten, M., unpublished results.

[73] Born, S.; Venzago, C.; Stojanik, B. *Appl. Spectrosc.*, 1998, **52**, 1358–1360.

[74] Graves, D. B.; Jensen, K. F. *IEEE Trans. Plasma Sci.*, 1986, **14**, 78–91.

[75] Passchier, D. *PhD Dissertation*, University of Utrecht, 1994.

[76] Kennis, P. *PhD Dissertation*, University of Antwerp, 1996.

[77] Ferreira, N. P.; Strauss, J. A.; Human, H. G. C. *Spectrochim. Acta, Part B*, 1982, **37**, 273–279.

[78] Steers, E. B. M.; Fielding, R. J. *J. Anal. At. Spectrom.*, 1987, **2**, 239–244.

[79] Hagstrum, H. D. *Phys. Rev.*, 1954, **96**, 325–335.

[80] Gill, P.; Webb, C. E. *J. Phys. D*, 1977, **10**, 299–311.

[81] Donko, Z.; Bano, G.; Szalai, L.; Kutasi, K.; Rosza, K.; Pinheiro, M.; Pinhao, N. *J. Phys. D.*, 1999, **32**, 2416–2425.